Surface instabilities in shock loaded granular media

K. Kandan[a,b], S. Khaderi[a,c], H.N.G. Wadley[d] & V.S. Deshpande[a*]

[a] *Department of Engineering, University of Cambridge, Trumpington Street, Cambridge CB2 1PZ, UK.*

[b] *School of Engineering, De Montfort University, The Gateway, Leicester LE1 9BH, UK.*

[c] *Department of Mechanical and Aerospace Engineering, Indian Institute of Technology Hyderabad, Yeddumailaram - 502 205, Telangana, India.*

[d] *Department of Material Science & Engineering, School of Engineering and Applied Science, University of Virginia, Charlottesville, VA 22904, USA.*

Abstract

The initiation and growth of instabilities in granular materials loaded by air shock waves are investigated via shock-tube experiments and numerical calculations. Three types of granular media, dry sand, water-saturated sand and a granular solid comprising PTFE spheres were experimentally investigated by air shock loading slugs of these materials in a transparent shock tube. Under all shock pressures considered here, the free-standing dry sand slugs remained stable while the shock loaded surface of the water-saturated sand slug became unstable resulting in mixing of the shocked air and the granular material. By contrast, the PTFE slugs were stable at low pressures but displayed instabilities similar to the water-saturated sand slugs at higher shock pressures. The distal surfaces of the slugs remained stable under all conditions considered here. Eulerian fluid/solid interaction calculations, with the granular material modelled as a Drucker-Prager solid, reproduced the onset of the instabilities as seen in the experiments to a high level of accuracy. These calculations showed that the shock pressures to initiate instabilities increased with increasing material friction and decreasing yield strain. Moreover, the high Atwood number for this problem implied that fluid/solid interaction effects were small, and the initiation of the instability is adequately captured by directly applying a pressure on the slug surface. Lagrangian calculations with the directly applied pressures demonstrated that the instability was caused by spatial pressure gradients created by initial surface perturbations. Surface instabilities are also shown to exist in shock loaded rear-supported granular slugs: these experiments and calculations are used to infer the velocity that free-standing slugs need to acquire to initiate instabilities on their front surfaces. The results presented here, while in an idealised one-dimensional setting, provide physical understanding of the conditions required to initiate instabilities in a range of situations involving the explosive dispersion of particles.

Keywords: Granular material; Fluid-structure interaction; Rayleigh-Taylor instability; shock loading

* Corresponding author. E-mail address: vsd@eng.cam.ac.uk

1. Introduction

So-called jetting or fingering instabilities involving jets of particles are widely observed in phreatic volcanic eruptions, the detonation of landmines, shallow underwater explosions, and during thermobaric explosions. A common feature in all these examples is high dispersion speeds with particle jets acquiring velocities significantly higher than the average speed of the dispersal front. The understanding of the formation and nature of these jets is of interest not only from a scientific viewpoint but is also of practical interest. For example, volcanic ash jets significantly increase the area over which ash is dispersed while the granular jets in landmine explosions are a significant contributor to damage in the impacted structures.

There have been several recent efforts to perform controlled experiments (Frost and Zhang, 2006; Ritzel et al. 2007; Zhang et al. 2010) to understand the basic phenomenology of these jetting instabilities. Some of the key insights gained from these studies can be summarized as follows. The dispersion of the particles depends on the velocity acquired by the particles (Frost et al., 2010), which in turn is a function of the ratio of the particle to explosive mass. The experiments of Frost et al. (2010) showed that there exists a minimum velocity for the jetting instability to initiate while Kyner et al. (2016) demonstrated that the jet velocities can be 50% greater than that of the main dispersal front.

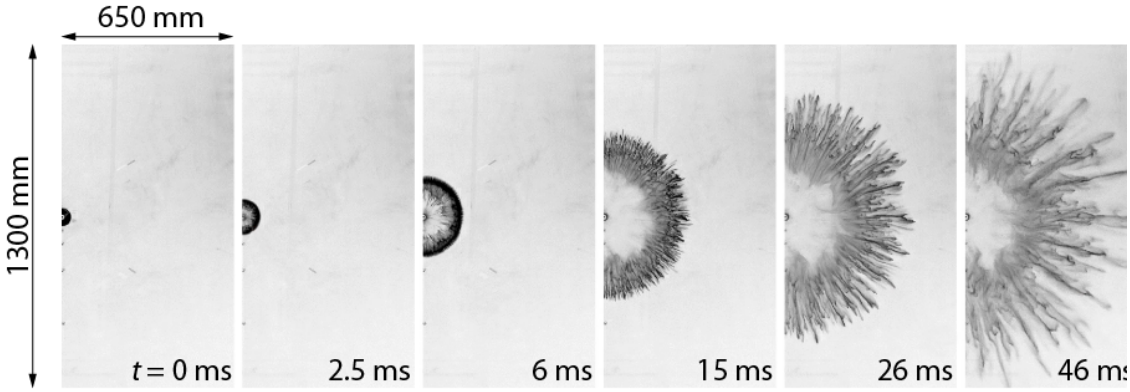

Figure 1: Sequences of high-speed photographs showing the cylindrical explosive dispersion of a granular medium comprising flour particles ~ 15 μm in diameter (Rodriguez et al., 2014).

Experiments such as those of Kyner et al. (2016) and Liu et al. (2014) have been out in spherical and planar configurations, respectively wherein only the outer surface of the granular front was visible. Experiments have also been reported in a cylindrical configuration wherein both the expanding gas/granular medium and granular medium/atmospheric air interfaces are visible (Frost et al. 2012; Rodriguez et al., 2014). High-speed photographs of the cylindrical expansion of a granular medium comprising of ~15 μm diameter flour particles are reproduced in Fig. 1 (Rodriguez et al., 2014). These experiments show the formation of instabilities on both interfaces with the expanding gas/granular medium interface becoming unstable early in the time-history. Stable particle jets are seen after 2.5 ms at the expanding gas/particle interface and at 15 ms after the start of the expansion event on the granular medium/atmospheric interface surface. Frost et al. (2012) also reported that water saturation of the granular medium produces more jets compared to a dry granular medium. In fact, the dispersion of water without particles produces many more jets of

liquid droplets (Cole, 1948) compared to dry or water-saturated granular media as noted by Frost et al. (2012).

The precise nature and causes of the instabilities responsible for jet formation at both interfaces remains a topic of active research. Ripley et al. (2012) focused attention on Richtmyer-Meshkov (Richtmyer, 1960) type instabilities (RMI), and demonstrated the formation of well-defined persistent jetting structures. However, the timescale for their formation was slow, and the surface instability did not propagate into the bulk. Milne et al. (2010) counted the number of jets and suggested a possible connection with dynamic fragmentation (Grady, 1982) while Frost et al. (2011) evaluated a compaction Reynolds number to connect expansion inertia to viscous dissipation. Discrete particle numerical calculations of Xu et al. (2013) suggest that particle jetting can be induced due to two sources: (i) the explosive gas forming jets induced by the shock wave propagating through the particle layers that the explosive gas is in contact with, and (ii) inelastic collisions between particles. However, multiphase numerical simulations by Zhang et al. (2013) suggest that the jets are connected to radial fractures in the fluid/granular medium. Thus, no consistent understanding of the physics of jet formation, and especially the influence of granular material properties (such as the influence of water) currently exists.

1.1 Scope of study

The aim of the study reported here is to develop a fundamental physical understanding of the mechanisms resulting in the formation of instabilities in shock loaded granular media. We thus report laboratory-scale shock tube experiments wherein the loading is well characterised and the initiation and growth of instabilities monitored in detail via high spatial and temporal resolution photography. Experiments are reported on both dry and water-saturated sand as well as a granular medium comprising PTFE spheres in order to span a wide range of granular material properties. These experiments are complimented with both Eulerian fluid/solid interaction simulations and Lagrangian direct pressure loading simulations. The simulations are used to construct maps that relate a stability criterion to loading conditions and material properties as well as to provide mechanistic insights into the origin of these instabilities.

2. Materials and experimental protocol

The explosive loading problem described in Section 1 is complex with the precise loading imposed by the expanding gases typically unknown. Moreover, the detailed temporal visualisation of the instabilities on both the high-pressure gas/granular media and granular media/atmospheric air interfaces is complicated as these experiments are typically performed in an outdoor setting where controlling lighting and other experimental parameters is difficult. Here we develop a *one-dimensional* laboratory-based model system to observe and investigate the mechanics of these instabilities.

The basic idea of the laboratory-based setup to investigate high-pressure gas shock loading of granular media is sketched in Fig. 2. A stationary granular slug is placed within a transparent tube that it is open at one end (at the right here) to atmospheric pressure such that the air in contact with the right face of the slug is stationary and at

atmospheric pressure and ambient temperature p_0 and T_0, respectively prior to the motion of the slug. A normal shock with pressure and temperature p_i and T_i, respectively is introduced at the far left end of the tube with the air in contact with the left face of the granular slug being stationary and at atmospheric conditions prior to the arrival of the shock. Given the shock pressure p_i and atmospheric upstream conditions, the normal shock relations (Liepmann and Roshko, 2001) for an ideal gas give the shock speed c_i as

$$\frac{c_i}{a_0} = \sqrt{\frac{\gamma - 1 + (\gamma + 1)\overline{p}_i}{2\gamma}}, \tag{2.1}$$

where $\overline{p}_i \equiv p_i/p_0$, γ is the ratio of specific heat capacities and $a_0 \equiv \sqrt{\gamma \overline{R} T_0}$ is the upstream sonic velocity (i.e. sonic velocity in atmospheric pressure air at ambient temperature) in terms of the specific gas constant $\overline{R}$. The sonic velocity a_i in the shocked (downstream) air is then

$$\frac{a_i}{a_0} = \sqrt{\frac{\overline{p}_i[\gamma + (\gamma - 1)\overline{p}_i]}{\gamma - 1 + (\gamma + 1)\overline{p}_i}}, \tag{2.2}$$

while the temperature and density of the shocked air are $T_i = a_i^2/(\gamma\,\overline{R})$ and $\rho_i = p_i/(\overline{R}T_i)$, respectively with the particle velocity within the shocked air given by

$$\frac{u_i}{a_0} = \sqrt{\frac{2(\overline{p}_i - 1)^2}{\gamma[\gamma - 1 + (\gamma + 1)\overline{p}_i]}}. \tag{2.3}$$

The normal shock travelling with velocity c_i impinges on the left end of the slug and reflects. This impinging shock accelerates the slug, which in turn pushes against the ambient air. This situation is reminiscent of the events outlined in Section 1 where the denotation of an explosive generates a high-pressure shock that accelerates the surrounding granular media into atmospheric air. However, in this controlled one-dimensional laboratory setting it is possible to make detailed high-speed photographic observations of the evolution of the slug within the transparent tube and identify any instabilities that might develop at both the high-pressure and ambient air interfaces of the granular slug.

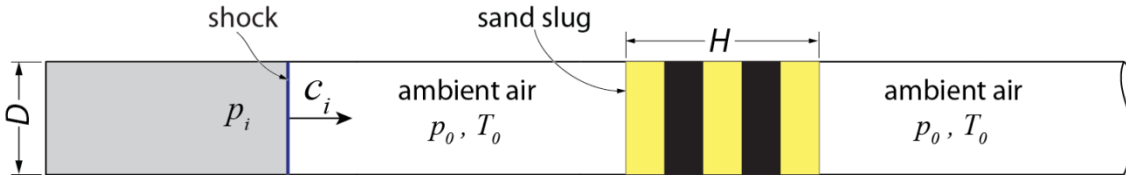

Figure 2: Sketch illustrating the principal of the one-dimensional transparent air shock tube for loading of granular slugs.

2.1 Granular materials & slug preparation

Two types of particles were used to construct granular slugs of height $H = 39$ mm and diameter $D = 28.5$ mm: (i) Silica particles (BS 1881-131:1998, fraction D) with

a nominal particle size range of $100 - 300\ \mu$m (we will subsequently refer to these particles as sand) and (ii) PTFE spheres with an average diameter $650\ \mu$m. We report experiments on both dry and water saturated sand slugs while PTFE slugs were only investigated in the dry state.

The slugs were prepared within a polycarbonate (PC) tube of length ~ 1m and inner and outer diameters of 28.5 mm and 32 mm, respectively by appropriately modifying a procedure introduced by Park et al. (2013) and Uth and Deshpande (2014). This procedure is briefly outlined here. The PC tube was thoroughly cleaned with soap water to improve visibility during the high-speed photography and an anti-static spray applied to the inside of the tube. One face of a 25 mm long cylindrical Nylon plug of diameter 28 mm was coated with a non-stick film and the plug inserted into the PC tube, coated face first. The tube was then aligned vertically with the plugged end at the bottom. We now proceed to explain the procedure used to prepare the dry sand slugs and then describe the modifications made to this procedure for the other two types of slugs.

Finely powdered sugar (0.04 g) was poured into the tube and spread evenly over the non-stick film on the Nylon plug. A few drops of water were then sprayed to moisten the sugar and 8 g of sand poured into the PC tube in 5 equal layers each of height ~ 8 mm. After pouring each layer, a 28.4 mm Nylon rod was inserted into the tube and dropped several times to compact the layer. The sand in the 2nd and 4th layer was dyed black (Park et al., 2013) to give a "zebra" appearance to the slug: this appearance aids the visualisation of the instabilities and the mixing of the air shocks and the granular media. After pouring and compaction of the final layer, 0.04 g of sugar was again poured and sprayed with water. The whole assembly was then dried for 4 hours under ultraviolet light. This dried the moist sugar and provided a very thin and brittle coating on the faces of the slug so that the slug maintained its shape when the PC tube was laid horizontal. The Nylon plug at the bottom of the tube was then removed and the assembly mounted horizontally into the air shock tube apparatus described in Section 2.2.

The PTFE slugs were prepared in an identical manner in 5 layers except that alternate layers were not dyed since the paints did not adhere to PTFE. Thus, the PTFE slug did not have the zebra appearance. The water-saturated sand slugs were also prepared in manner similar to the dry sand slugs with two exceptions: (i) surface tension due to the water was sufficient to maintain the slug shape in the horizontal position so that no sugar was required, and (ii) after pouring and compaction all the 5 layers to create the zebra slug, 8.92 g of water was poured into the PC tube and allowed to slowly infiltrate the porosity within the slug under the influence of gravity. The 8.92 g of water was exactly the amount required to just fill the interstices between the particles of the compacted dry sand slug and a fully water-saturated sand slug was thus obtained.

The Young's modulus E, Poisson's ratio ν, cohesive strength Y, friction angle φ and overall density ρ_{slug} of the three types of granular slugs are summarised in Table 1. A brief description of the methods used to estimate these mechanical properties is included in the Appendix A. We emphasize here that the PTFE sphere slugs were chosen especially due to their low moduli and friction, which results in a different regime of behaviour, as will be discussed in Sections 3 and 4.

Material	Young's modulus E (MPa)	Friction angle φ (degrees)	Yield strength Y (kPa)	Density ρ_{slug} (kgm^{-3})
Dry sand	100	23	0.25	1650
Water-saturated sand	250	0	0.625	2000
PTFE	0.18	5	1.8	880

Table 1: Summary of the material properties of the three granular slugs investigated here. The Poisson's ratio $\nu = 0.49$ for all cases. All slugs had a diameter $D = 28.5$ mm and length $H = 39$ mm.

2.3 Experimental protocol for air shock loading

The air shock loading was applied via a single stage gas gun comprising a high pressure gas cylinder, a double shim breach and a 2.25 mm long steel barrel of inner diameter 28.5 mm. The PC tube was fitted into the end of the steel barrel such that the inner surfaces of the PC and steel tube were flush as shown in Fig. 3a. Two dynamic pressure sensors (Piezotronics ICP pressure sensor 134A22) were fitted towards the end of the steel tube one 85 mm behind the rear end of the granular slug and another one a further 1865 mm further back (the granular slug was within the PC tube as shown in Fig. 3a). The sensors measured the gauge pressure at their respective location. For the sake of brevity, we only report pressure measurements from the sensor closest to the slug with the second sensor only used to verify that the normal shock relations were satisfied including the shock speed relation, Eq. (2.1).

The air shock was introduced into the system using a double shim approach to ensure that a sharp shock impacted the granular slugs. With copper shims sealing both ends of the breach as shown in Fig. 3a, the pressure cylinder was filled with Nitrogen gas to a gauge pressure P_c via inlet 1 while the breach was simultaneously also pressurised with Nitrogen via inlet 2 to a pressure $P_c/2$. Solenoid valves fitted on inlet 1 and 2 isolated these pressure chambers and enclose a volume ~ 0.02 m^3 within the main pressure cylinder (the breach volume is negligible compared to the main pressure cylinder). A photograph of the pre-bulged copper shim with 4 symmetric scoring marks used to seal the breach is included in Fig. 3b. The scoring depth was designed for each value of P_c used in experiments such that the shim ruptured by a petalling mechanism (Fig. 3c) when the pressure differential across it exceeded $3P_c/4$. To trigger the shock, the solenoid valve on inlet 2 was opened allowing the pressure in the breach to drop to the atmospheric condition. This resulted in the pressure differential across shim separating the breach and the pressure cylinder exceeding $3P_c/4$ and shim rupture. A shock then travelled down the breach and burst the second shim resulting in a normal shock that propagated along the barrel towards the granular slug. The petalling failure mechanism of the shims also ensured that that no failed shim debris was carried with that shock.

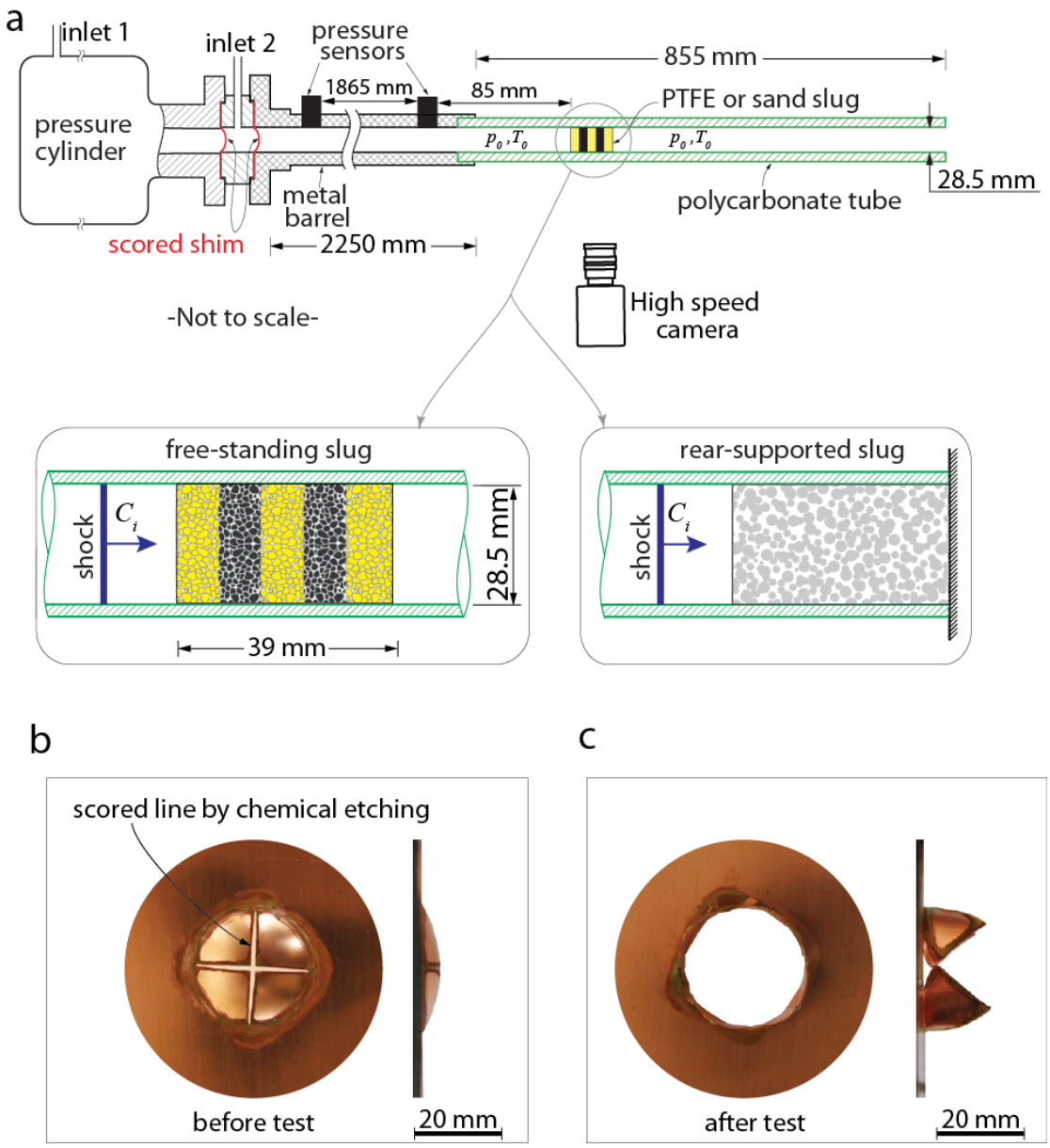

Figure 3: Sketch of the experimental setup for shock loading of granular slugs. (a) The overall setup comprising a high-pressure cylinder, the breach, and a PC tube holding the granular slug. The two insets show details of the "zebra" striped water-saturated and dry sand free-standing slugs and the rear-supported PTFE slug. All dimensions are in mm. Photograph of a 0.25 mm thick scored copper shim used in the breach of the shock tube (b) before and (c) after test. The 0.25 mm shim was used for loading with a cylinder pressure $P_c = 6.1$ MPa.

Tests were conducted with absolute cylinder pressures in the range $0.24\ \text{MPa} \leq P_c \leq 7.3\ \text{MPa}$ and the ambient atmospheric conditions were fixed at $p_0 = 0.1$ MPa, and $T_0 = 298$ K. To a high degree of accuracy $\gamma = 1.4$ and $\overline{R} = 287\ \text{J kg}^{-1}\text{K}^{-1}$ since Nitrogen and ambient air have approximately the same ratio of specific heat capacities and density. A typical absolute pressure versus time history measured by the sensor with $P_c = 6.1$ MPa and the barrel capped by a rigid and stationary plug at a distance of $d = 85$ mm from the pressure sensor is plotted in Fig. 4. Here time $t = 0$ is defined as the time when the shock wave arrives at the pressure sensor. A sharp

shock with $\overline{p}_i = 5.5$ is observed and from Eq. (2.1) we deduce that the shock speed is $c_i = 588\ \mathrm{ms}^{-1}$. This shock then impinges on the rigid plug at $t = d/c_i \approx 0.14$ ms and is reflected with a pressure p_r given by (Taylor, 1940)

$$\frac{\left(\overline{p}_r/\overline{p}_i - 1\right)^2}{\gamma - 1 + (\gamma+1)\overline{p}_r/\overline{p}_i} = \frac{\left(\overline{p}_i - 1\right)^2}{\overline{p}_i\left[\gamma + 1 + (\gamma-1)\overline{p}_i\right]}, \tag{2.4}$$

where $\overline{p}_r \equiv p_r/p_0$, giving $\overline{p}_r = 20.5$ for $\overline{p}_i = 5.5$. The measured reflected shock pressure is marked in Fig. 4 and is in reasonable agreement with this prediction. The reflected shock travels back from the rigid plug towards the sensor with a shock wave speed c_r relative to the un-shocked air given by

$$\frac{c_r}{u_i} = \frac{\gamma - 1 + (\gamma+1)\,\overline{p}_r/\overline{p}_i}{2(\overline{p}_r/\overline{p}_i - 1)}, \tag{2.5}$$

and is expected to arrive at the sensor at time $t = d/c_i + d/c_r$. Substituting from Eqs. (2.3) and (2.5) we estimate the reflected shock arrives at the sensor at $t = 0.27$ ms in agreement with the data in Fig. 4. Shortly after the arrival of the reflected shock there is another sudden increase in the pressure measured by the sensor. This corresponds to the arrival of the contact surface between the original high pressure Nitrogen gas within the pressure cylinder and the atmospheric air within the barrel. The pressure then rises to approximately 6 MPa (i.e. the initial pressure within the high-pressure cylinder), since the volume of the capped barrel ($\sim$1.43 dm^3) is much smaller than that of the pressure cylinder ($\sim$0.02 m^3).

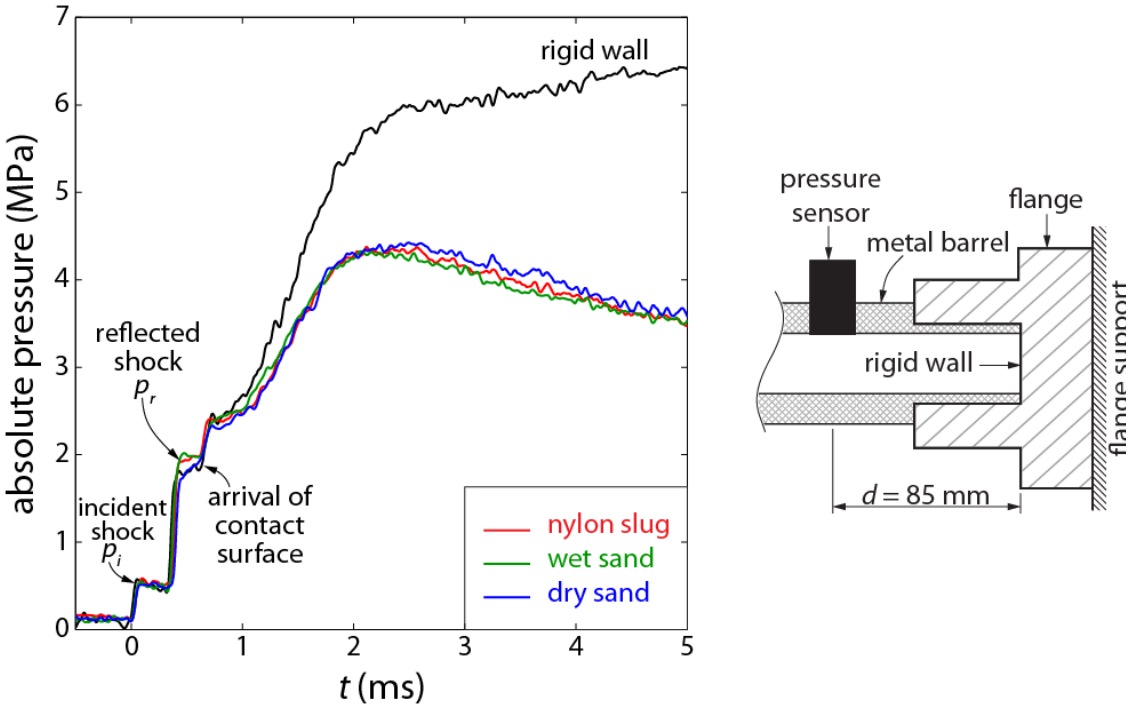

Figure 4: The measured absolute pressure histories within the shock tube as a function of time t for a cylinder pressure $P_c = 6.1$ MPa. Here $t = 0$ corresponds to the instant that the incoming shock first reaches the pressure sensor that is located 85 mm behind the face of the

stationary slug impinged by the shock wave. Readings are reported for three slugs: the water-saturated sand, dry sand and a solid Nylon slug of the same overall dimensions and mass as the water-saturated sand slug. The pressure history in a capped tube (rigid wall) with $P_c = 6.1$ MPa is also included. The inset in the figure shows a sketch of the capped end of the tube with the location of the pressure sensor.

This data confirms that the initial shock loading imposed by this apparatus corresponds to that in a standard shock tube as given by the normal shock relations. However, at longer time scales the initial pressure within the high-pressure cylinder better approximates the pressure loading.

Cylinder pressure P_C (MPa)	Incident pressure p_i (MPa)	Free-standing			Rear-supported
		PTFE	Dry Sand	Water-saturated Sand	PTFE
0.24	0.13	S	-	-	-
1.6	0.41	U	S	U	S
3.0	0.43	U	S	U	-
6.1	0.55	U	S	U	U
7.3	0.59	-	-	-	U

Table 2: Test matrix showing the range of cylinder pressures and corresponding incident pressures measured at the sensor location illustrated in Fig. 3a. In the table "U" and "S" denotes observed unstable and stable responses, respectively while the – indicates no test performed under those conditions.

3. Observations of instabilities in free-standing slugs

We proceed to discuss observations of the evolution of the shock loaded granular slugs via high-speed photography using a Phantom v16 (Vision Research) camera equipped with a macro lens (Makro-Killar 2.8/90) and matched multiplier (Vivitar 2x). Four flash lights were used for illumination and images were taken with an inter-frame time of $11.21\mu s$ and an exposure time of 0.43 μs.

3.1 Instabilities in sand slugs

High-speed photographs of a evolution of the dry and water-saturated sand slugs are shown in Figs. 5a and 5b, respectively for shock loading generated with a cylinder pressure $P_c = 6.1$ MPa: this generates a shock of magnitude $\overline{p}_i = 5.5$ as seen in Fig. 4. In the montage in Fig. 5, time $t_i = 0$ corresponds to the instant the incoming shock first impinges on the surface of the slug. The dry sand slug moved approximately as a rigid body until it reached the end of the PC tube (some disturbance at the front end of the slug is seen at $t_i \approx 3.7$ ms). By contrast, the initiation of surface instabilities on the face of the water-saturated sand slug impinged by the shock is seen at $t_i \approx 0.8$ ms. This instability grows and propagates into the water-saturated sand slug resulting in both mixing of the granular media and the shocked air as well as significant

lengthening of the slug[1]. The test conditions for all the tests performed in this investigation are summarised in Table 2. Over the entire range of P_c values considered, an instability was always observed on the face of the water-saturated sand slug impinged by the incoming shock while no clear instability was observed in any of the dry sand slug experiments.

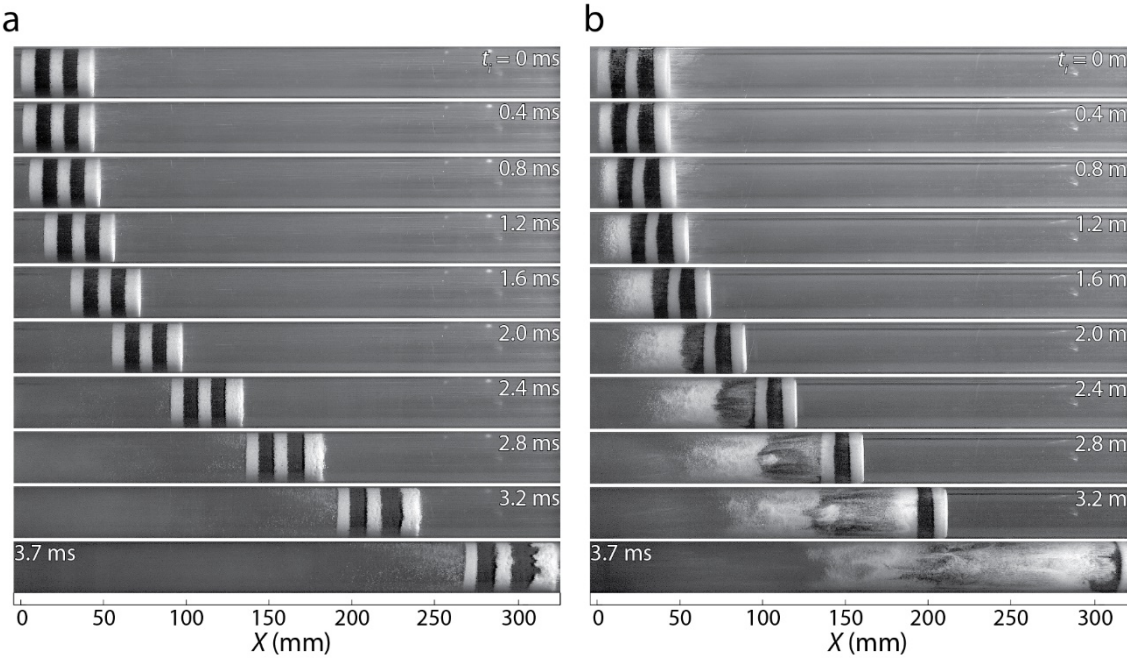

Figure 5: Montage of high-speed photographs showing the evolution of the (a) dry and (b) water-saturated sand slugs loaded by a $\overline{p_i} = 5.5$ shock wave (cylinder pressure $P_c = 6.1$ MPa). Here time $t_i = 0$ corresponds to the instant the incoming shock first impinges on the surface of the slug.

[1] We emphasize that over the approximately 3 ms time scale of the experiment, the high-speed photographs have confirmed that the water-saturated sand slug remained in an undrained state with no leakage of water from the slug.

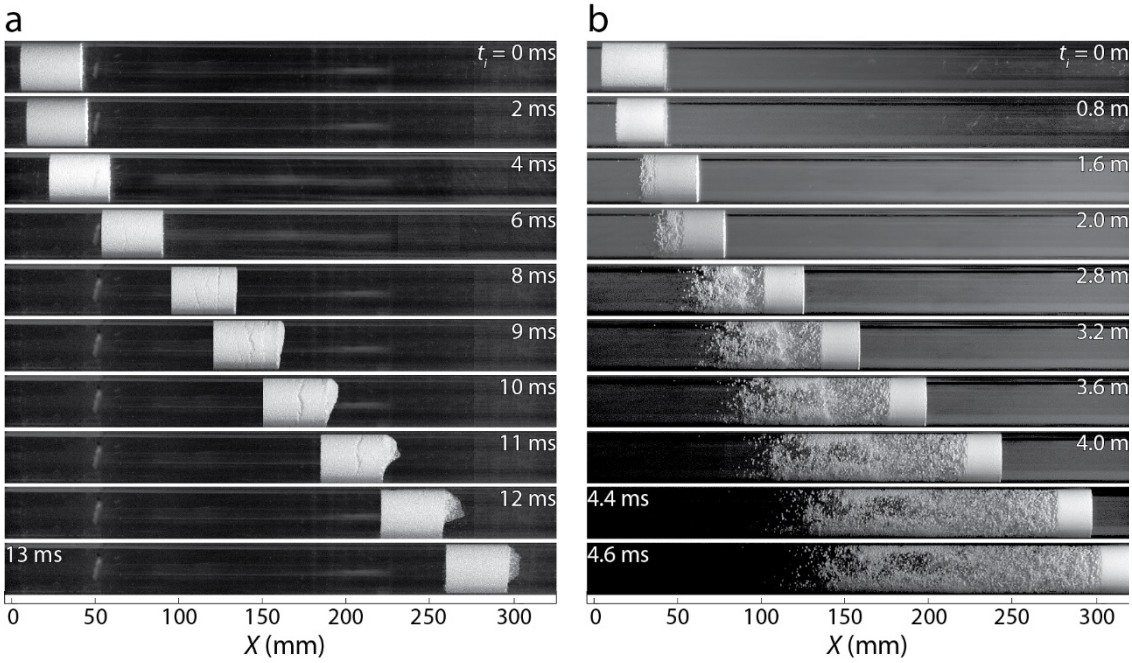

Figure 6: Montage of high-speed photographs showing the evolution of the PTFE sphere slugs loaded by a (a) $\overline{p}_i = 1.3$ ($P_c = 0.24$ MPa) and (b) $\overline{p}_i = 4.1$ ($P_c = 1.6$ MPa) shock wave. Here time $t_i = 0$ corresponds to the instant the incoming shock first impinges on the surface of the slug.

One possible explanation for these differences in the water-saturated and dry sand slug responses is that the fluid/solid interaction differs in the two cases, i.e. the resultant loading due to the imposed air shock is different for the dry and water-saturated sand slugs. For example, the porosity within the dry sand slug might allow the air shock to penetrate into the slug thus lowering the applied pressure while the water saturating the pores in the water-saturated sand slug precludes this possibility. To test this hypothesis, measurements of the temporal pressure history for the water-saturated and dry sand slug experiments of Fig. 5 are included in Fig. 4. Similar to the measurements reported in Section 2.3, the pressure was measured by a sensor located 85 mm behind the stationary sand slugs. In addition, a $P_c = 6.1$ MPa shock loading experiment was performed with a Nylon slug of same overall dimensions and mass as the water-saturated sand slug (a steel rod was inserted into the core of the Nylon slug so that the slug had both the same overall dimensions and mass as the water-saturated sand slug). All these measured pressure histories are included in Fig. 4 from which it is clear that both the incident and reflected pressure pulses are approximately the same for all three cases. This suggests that over the time-scale of the experiment, there is negligible leakage of air through the porosity within the sand slugs. The differences between the responses of the water-saturated and dry sand slugs are therefore due only to differences in material properties of the water-saturated and dry sand (and not due to differences in the resultant loading on the slugs).

3.2 Instabilities in PTFE sphere slugs

To further understand the effect of material properties on the stability of pressure loaded granular slugs, experiments were performed on slugs (also included in Table 2) made from PTFE spheres. These slugs were in the dry state but had material properties rather different from the dry sand; see Table 1.

Montages of high-speed photographs of the PTFE sphere slugs impinged by shocks generated with $P_c = 0.14$ MPa and 1.5 MPa are shown in Figs. 6a and 6b, respectively. These cylinder pressures generate incident normal shocks with $\overline{p}_i = 1.3$ and 4.2, respectively. Over the duration of the experiment, no instability was observed in the $\overline{p}_i = 1.3$ case (similar to the dry sand slug some disturbance is observed at the front end of the slug towards the end of the experiment). By contrast, there is clear instability that initiates at $t_i \approx 1.6$ ms on the face of the slug impinged by the $\overline{p}_i = 4.2$ shock (Fig. 6b). Similar to the water-saturated sand slug, this results in mixing between the granular media and the shocked air accompanied by lengthening of the slug.

These the experiments on the sand (water-saturated and dry) and PTFE sphere slugs suggest that instabilities can develop on the face of a granular slug impinged by air shock. The conditions required to trigger these instabilities depend on the material properties of the granular medium (with water within the pores not essential) and the magnitude of the imposed shock loading.

4. Simulations of air shocks interacting with granular slugs

Simulation of the shock loading of granular slugs are now reported in order to provide some understanding of the parameters that govern the onset of the instabilities observed in the experiments. The results presented in Section 3 show that the imposed loading is well approximated by a normal shock with pressure p_i for the time-scales over which these instabilities are initiated (though their evolution takes place over longer time scales). Since the focus here is on investigating the initiation of these instabilities, it suffices to only model the initial normal shock loading phase and neglect the subsequent static loading due to the slow flow of the gas from the pressure cylinder.

4.1 Model setup

An Eulerian model setup, sketched in Fig. 7, was employed to investigate the interaction between the granular slug and the shock with incident pressure p_i. The shock tube was modelled as a long rectangular tube of length L_{tube}, width D and unit depth. At time $t = 0$, the granular slug (unit depth) occupied a region of size $H \times D$ within the shock tube as shown in Fig. 7 with stationary (ambient) air with pressure p_0, temperature T_0 and density ρ_0 on either side of the slug. A geometric imperfection in the form of a sinusoidal wave of amplitude A and wavelength λ was imposed on the surfaces of the granular slug such that the mean length of the slug is H. This perturbation was required to trigger instabilities during the numerical calculations.

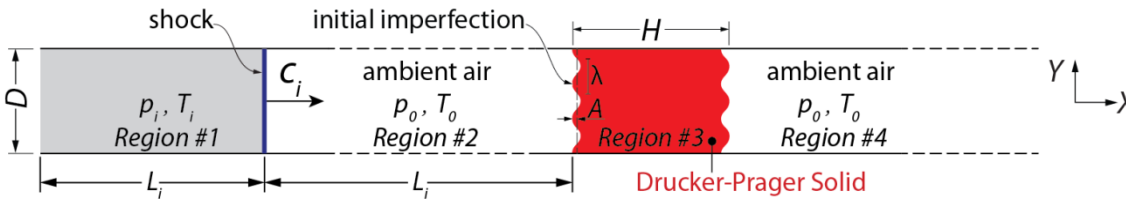

Figure 7: Sketch of the shock tube setup used in the Eulerian calculations. At time $t = 0$ there are 4 regions with the granular slug occupying region 3 and the shocked air in region 1. The geometric imperfections on the slug surfaces are indicated along with the global (X,Y,Z) co-ordinate system employed.

An incoming shock with pressure p_i was introduced within the shock tube such that at time $t = 0$ the shock front was at a distance L_i from the left end of the shock tube and the same distance from the granular slug. The particle velocity u_i, shock velocity c_i, temperature T_i and density ρ_i in the shocked region are related to p_0, ρ_0 and T_0 via the equations in Section 2. Thus, at time $t = 0$ the shock tube is divided into the four regions shown in Fig. 7 with the incoming shock travelling towards the granular slug with a velocity c_i. This incoming shock impinged on the granular slug and accelerated it. The moving granular slug in turn compressed the air in front of it. The simulations were terminated prior to this compressed air front reaching the right end of the shock tube of length L_{tube} (the tube may thus be considered to be infinitely long for the purposes of the simulations). All simulations reported here were performed via an Eulerian solver: it is worth mentioning that other techniques such as Arbitrary Lagrangian-Eulerian (ALE) and Discrete Particle Methods (DPM) are available as alternatives. While ALE is expected to give similar results, discrete particle effects that might become significant as the instability grows can be accounted for via DPM. Such calculations are beyond the scope of this study.

The simulations were performed using the Eulerian solution capability of the commercial finite element code ABAQUS. The domain was discretised using 8-noded 3D bricks with reduced integration (EC3D8R in ABAQUS notation). Elements of size $0.007H$ were used to discretise the domain in the $X-Y$ directions (see Fig. 7) while only one element was used to discretise in the $Z-$ direction so as to simulate a plane strain situation as discussed below. The temporal discretization was carried out using a forward Euler scheme (explicit dynamic method) and the evolution of the interfaces between the different regions in Fig. 7 was captured using the volume of fluids method (Hirt and Nichols, 1981). With (u_X,u_Y,u_Z) and (t_X,t_Y,t_Z) denoting the velocities and tractions in (X,Y,Z) directions, respectively the following boundary conditions were imposed on the Eulerian mesh:

(i) Plane strain conditions[2] were imposed by specifying $u_Z = 0$ on all nodes.

(ii) At the left inlet we impose velocities $(u_i,0,0)$ to simulate the incoming shock while at the right outlet the velocities $(0,0,0)$ were imposed to simulate the stationary ambient air conditions.

(iii) Along the surfaces of the shock tube at $Y = \pm D/2$ we impose the velocity $u_Y = 0$ and the traction $t_X = 0$ to simulate frictionless conditions.

In addition, the initial conditions at time $t = 0$ specified over the four regions are:

[2] A few scoping full three-dimensional (3D) calculations confirmed that the plane strain assumption predicted the onset of the instability to within 3% accuracy. Thus, in order to reduce the numerical cost associated with the computing the stability maps presented subsequently, all calculations reported here assume plane strain conditions.

(i) Regions 2 and 4 were air at ambient pressure and temperature p_0 and T_0, respectively and velocity $(u_X,u_Y,u_Z) = (0,0,0)$.

(ii) Region 3 was the granular media with constitutive model specified in Section 4.2 and velocity $(u_X,u_Y,u_Z) = (0,0,0)$.

(iii) Region 1 was the initially shocked air at pressure p_i with the temperature and density within the region related to that in region 2 via the equations in Section 2. Moreover, the material within that region is given an initial velocity $(u_i,0,0)$ where u_i is related to p_i via Eq. (2.3).

4.2 Material properties

The air was modelled as an ideal gas under adiabatic conditions with $\gamma = 1.4$ and specific gas constant $\overline{R} = 287$ J kg^{-1}K^{-1}. The ambient conditions were $p_0 = 0.1$ MPa and $T_0 = 298$ K with the initial shocked region length was taken to be $L_i = 1.7$ m (this parameter has no influence on the results). The granular media was modelled as an isotropic elastic non-hardening (and rate independent) Drucker-Prager solid (Drucker and Prager, 1952) with Young's modulus E and Poisson's ratio ν. The Drucker-Prager yield condition is written in terms of the von-Mises stress $\sigma_e \equiv \sqrt{(3/2)s_{ij}s_{ij}}$, where s_{ij} is the deviatoric stress and hydrostatic pressure $p \equiv -\sigma_{kk}/3$ as

$$\sigma_e - \mu p - Y \leq 0, \tag{4.1}$$

where $Y/(1-\mu/3)$ is the uniaxial compressive strength of the granular material and μ is the friction co-efficient. Here we interpret Eq. (4.1) as the circumscribing yield surface to the Mohr-Coloumb yield surface and hence μ in terms of the friction angle φ measured via cone angle tests (Appendix A) is given by $\mu \equiv 2\sin\varphi/[\sqrt{3}(3-\sin\varphi)]$. Consistent with a wide body of experimental data on granular materials (Bolton, 1991), we assume that plastic straining is incompressible. Therefore, we employ a non-associated flow rule with the plastic strain rate $\dot{\varepsilon}_{ij}^p$ under active yield conditions given in terms of the plastic multiplier κ as

$$\dot{\varepsilon}_{ij}^p = \kappa \frac{\partial \sigma_e}{\partial \sigma_{ij}}. \tag{4.2}$$

This constitutive model with $Y > 0$ is only valid for compressive hydrostatic stress states. All the shock-loaded slug cases analysed here satisfy this condition. The relevant material properties required for this model (including overall initial density) for the three types of granular media considered in this study are listed in Table 1. All calculations reported in this section employ an imperfection $A/\lambda = 0.01$ and $D/\lambda = 3.5$. The slug size is taken to match the experiments, viz. $H = 39$ mm and $D = 28.5$ mm.

It is worth emphasising here that the friction angle φ to be used in the Drucker-Prager model is best obtained from triaxial tests. However, such complex constitutive property tests are beyond the scope of this study that focuses on the dynamic instabilities. Nevertheless, we shall subsequently show that the stability conditions are

reasonably insensitive to φ over a wide range of the friction angles and hence estimating φ via cone angle tests is adequate for the purposes of this study.

4.3 Predictions of granular slug evolution under shock loading

Snapshots showing the predictions of the evolution of the dry and water-saturated sand slugs for shock loading with $\overline{p}_i = 5.5$ are included in Figs. 8a and 8b, respectively with time $t_i = 0$ corresponding to the instant the shock arrives at the granular slug/air interface. Similar to the experiments (Fig. 5), the dry sand slug retains its shape with negligible deformation over the period simulated. By contrast, instabilities initiate at $t_i \approx 1$ ms on the surface of the water-saturated sand slug impinged by the shock. This surface ripple at $t_i = 1$ ms grows forming fingers that eventually neck and break away from the slug resulting in mixing of the granular media and the shocked air similar to that observed in experiments. For the sake of brevity we do not report simulations for other shock conditions, but over the range of shock pressures employed in the experiments reported above, the water-saturated sand slug always had an unstable response while the dry sand slug remained stable consistent with experimental observations.

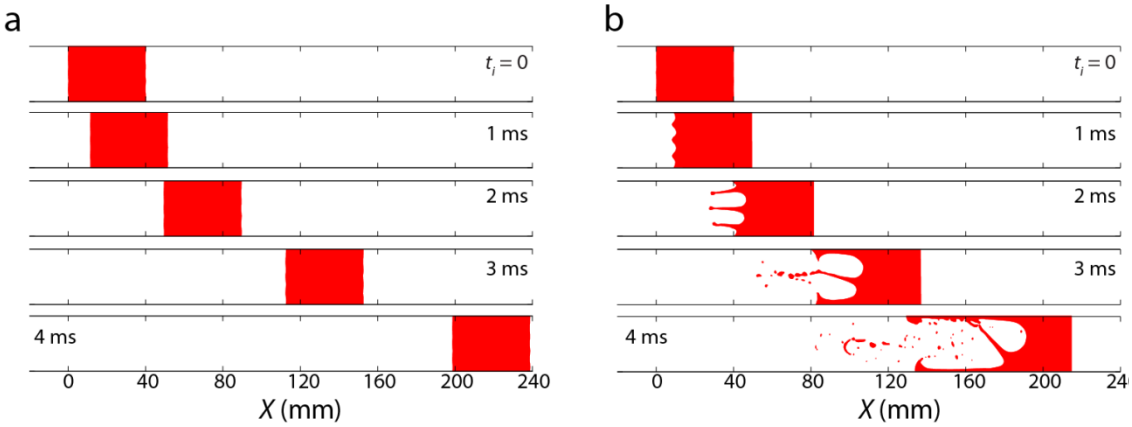

Figure 8: Snapshots of the slug shape from Eulerian simulations of the (a) dry and (b) water-saturated sand slugs loaded by an incoming normal shock of magnitude $\overline{p}_i = 5.5$. Here time $t_i = 0$ corresponds to the instant the incoming shock first impinges on the surface of the slug.

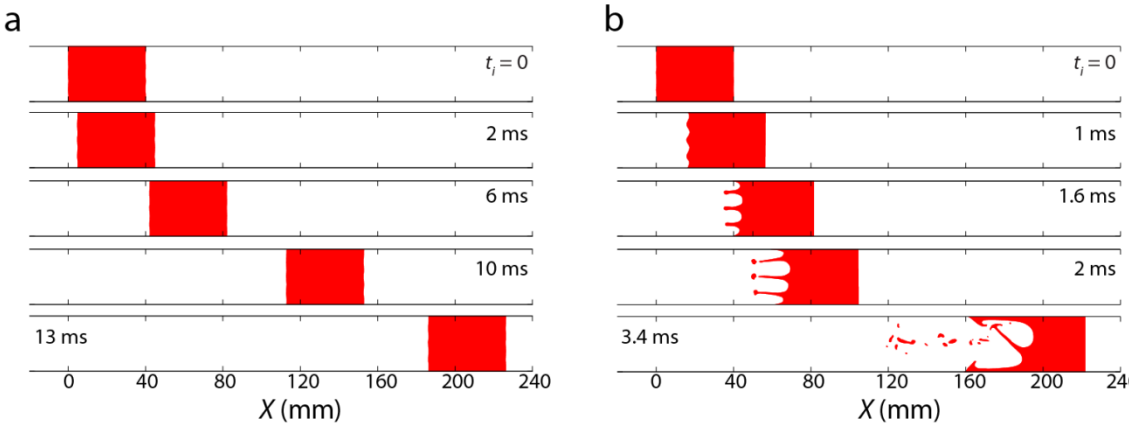

Figure 9: Snapshots of the slug shape from Eulerian simulations of the PTFE sphere slug loaded by normal shocks of magnitude (a) $\overline{p}_i = 1.3$ and (b) $\overline{p}_i = 4.1$. Here time $t_i = 0$ corresponds to the instant the incoming shock first impinges on the surface of the slug.

Simulation of the evolution of the PTFE slugs subjected to $\overline{p}_i = 1.3$ and 4.1 are included in Figs. 9a and 9b, respectively. Again similar to the experiments, the slug retained its shape and remained stable over the duration simulated for $\overline{p}_i = 1.3$. On the other hand, with $\overline{p}_i = 4.1$ instabilities developed on the surface of the slug impinged by the incoming shock. Then, like the water-saturated sand slugs, this instability grew to form fingers that eventually necked and resulted in mixing of the granular medium and the shocked air similar to the experiment; see Fig. 6b. It is emphasized here that in line with other dynamic instabilities (Abrahamson and Goodier, 1966), we expect the wavelength of the dominant imperfection (i.e. the imperfection that grows most rapidly) to be a function of the both the loading and material properties. Thus, the growth of the instability will depend on the choice of the imperfection. Such an investigation is beyond the scope of this current study whose focus is the initiation criterion rather than a prediction of the number and type of fingers formed. Moreover, the analysis implicitly assumes immiscibility of the air and the granular materials. While this is true early in the loading history (see Fig. 4 and discussion in Section 3.1), this assumption fails as the instability grows and the fingers break-up. In fact, the predictions of the break-up of the fingers in Figs. 8 and 9 are largely an artefact of the Eulerian simulation scheme and dependent on the mesh size used in the calculations. This remains a limitation of the analysis employed here.

We conclude that a relatively simple Drucker-Prager model for the granular media along with the appropriate material parameters captures many of the key experimental observations of the onset and even to some extent the evolution of the surface instabilities.

4.4 Stability maps

Recall that loading on the slug is well approximated by the pressure p_r resulting from the reflection of the incident shock from a rigid stationary wall; see Fig. 4 and Eq. (2.4). It is thus convenient to describe the stability criterion in terms of the minimum value of $(Y/p_r)_{\text{crit}}$ required to ensure a stable response. Dimensional analysis dictates that

$$(Y/p_r)_{\text{crit}} = f(\overline{p}_i, \hat{p}_r, \mu, \nu, \rho_{slug}/\rho_0), \tag{4.3}$$

where $\hat{p}_r \equiv p_r/E$ with $\overline{p}_r$ related to $\overline{p}_i$ via Eq. (2.4). We proceed to determine this functional form. Unless otherwise specified, we first report calculations in which the initial slug density was kept fixed at $\rho_{slug} = 2000$ kg m^{-3} with $\nu = 0.49$ (i.e. values for the water-saturated sand slug) with the incoming shock travelling through ambient air. The dependency on ν and ρ_{slug}/ρ_0 is relatively less important for the granular materials being considered here and only briefly discussed subsequently.

First consider the case of $\overline{p}_i = 5$ and $\hat{p}_r = 1.0$ (i.e. a Young's modulus $E = 2$ MPa). Calculations were performed for a range of values of the granular material yield strengths Y and friction co-efficient μ and the slug labelled as stable or unstable for each combination (Y,μ). In order to define stability, we plot the temporal evolution of the length of the slug surface impinged by the incoming shock with time $t_i = 0$ corresponding to the instant the shock wave first impinged on the slug. If this length

increased by more than 2% over a time period $0 \le t_i c_L/\lambda \le 20$, where $c_L = \sqrt{E/\rho_{slug}}$ is the longitudinal wave speed of the slug, then the case is said to result in an instability or otherwise classified as stable.

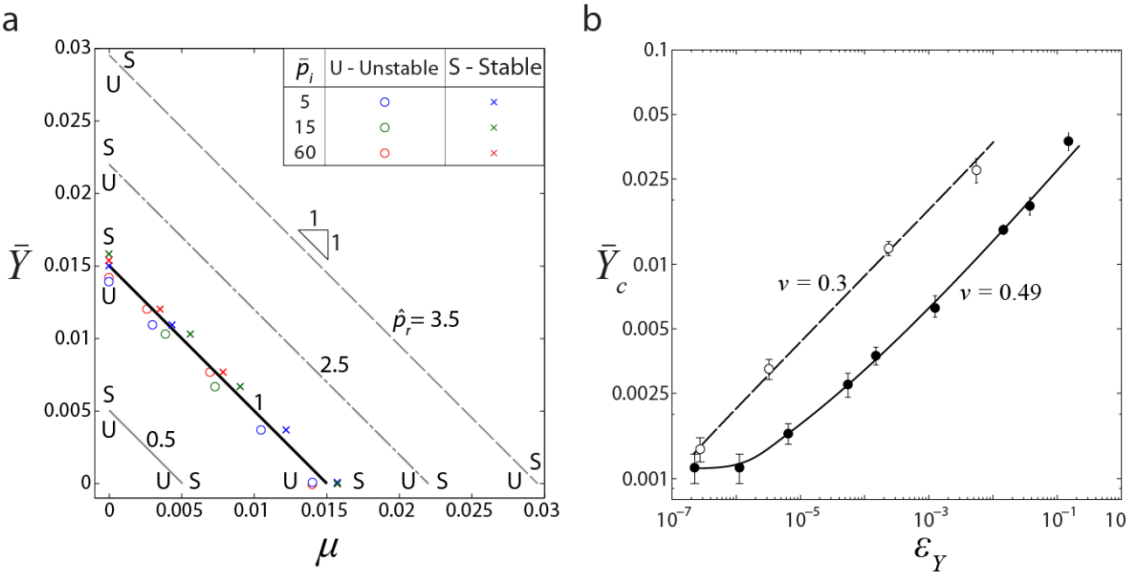

Figure 10: Stability of sand slugs with $A/\lambda = 0.01$, $D/\lambda = 3.5$ and $H/D = 1.4$. (a) Stability maps for slugs with $\nu = 0.49$ in $\overline{Y} - \mu$ space for four selected values of $\hat{p}_r$. (b) Predictions of the critical normalised strength $\overline{Y}_c$ of the frictionless material required to ensure stability of the slug as a function of its yield strain ε_Y. Results are shown in (b) for two choices of the Poisson's ratio $\nu = 0.49$ and 0.3.

Selected simulations giving stable (marked by a cross) and unstable responses (marked by a circle) are included in the map in Fig. 10a using axes of the normalised strength $\overline{Y} \equiv Y/p_r$ and the friction coefficient μ. The boundary between the stable and unstable regions is seen to be well approximately by a straight line in $\overline{Y} - \mu$ space. Now keeping $\hat{p}_r = 1.0$ we consider two additional incident shocks with $\overline{p}_i = 15$ and 60 (i.e. the Young's modulus E is increased in each case to keep $\hat{p}_r = 1.0$). Again a series of calculations were performed to determine the boundary between stable and unstable regimes in $\overline{Y} - \mu$ space and the results included in Fig. 10a. Remarkably all the data in Fig. 10a for loading specified by $\hat{p}_r = 1.0$ collapses on to a single straight line with a slope of -1, demarking the stable and unstable regimes, i.e. in $\overline{Y} - \mu$ space the dependency on $\overline{p}_i$ is negligible. The stability criterion can then be simply written as

$$\overline{Y} \ge \overline{Y}_0 - \mu, \tag{4.4}$$

with $\overline{Y}_0 = (Y/p_r)_{\text{crit}}$ at $\mu = 0$. Predictions of the boundary demarking the stable and unstable regimes for three additional values of $\hat{p}_r$ are included in Fig. 10a. With increasing $\hat{p}_r$, the unstable regime grows but over all loadings considered here the stability criterion is given by Eq. (4.4) with $\overline{Y}_0$ a function of $\hat{p}_r$. We note that the stability criterion (4.4) is of the same form as the Drucker-Prager yield criterion (4.1)

used to describe the yield condition of the granular material. This strongly suggests that the loss of stability of the slug is related a low effective strength of the granular material in comparison to the applied shock pressure. In particular, the low cohesive strength and frictionless behaviour of the (saturated) water-saturated sand is akin to liquefaction, although the water-saturated sand a-priori has a low strength rather than loosing strength on application of the pressure.

Given that the stability criterion (4.4) is a straight line in $\overline{Y}-\mu$ space with a slope of -1, the function $\overline{Y}_0$ fully describes the stability map in Fig. 10b. Recalling that the dependency on $\overline{p}_i$ is negligible, dimensional analysis again dictates that $\overline{Y}_0(\hat{p}_r,\nu,\rho_{slug}/\rho_0)$. This functional form contains a loading dependent parameter $\hat{p}_r$ that complicates interpretation in the context of a given material. It is thus more convenient to recast this functional form in terms of only material parameters, i.e. $\overline{Y}_c(\varepsilon_Y,\nu,\rho_{slug}/\rho_0)$ with $\varepsilon_Y \equiv Y/E$ the yield strain of the material. (We emphasize that $\overline{Y}_0$ and $\overline{Y}_c$ are the same functions with the different subscripts used to highlight the change of the independent variables.) This functional relation was determined by performing a series of calculations with $\mu = 0$ and varying the yield strain over a range $2\times10^{-7} \le \varepsilon_Y \le 0.1$. Predictions of $\overline{Y}_c(\varepsilon_Y,\nu)$ [3] for $\nu = 0.49$ and 0.3 are included in Fig. 10b with the error bars denoting the numerical range within which $\overline{Y}_c$ was determined. It is clear that $\overline{Y}_c$ increases with ε_Y but decreases with increasing ν as the material becomes nearly incompressible. We note in passing that given $\overline{Y}_0(\hat{p}_r,\nu)$, the yield strain of the material that is just stable for a loading $\hat{p}_r$ is $\varepsilon_Y = \overline{Y}_0(\hat{p}_r,\nu)\hat{p}_r$. Then via a change of variables, $\overline{Y}_c(\varepsilon_Y,\nu)$ follows from $\overline{Y}_0(\hat{p}_r,\nu)$, i.e. consistent with dimensional analysis, it is sufficient to specify either the function $\overline{Y}_0(\hat{p}_r,\nu)$ or $\overline{Y}_c(\varepsilon_Y,\nu)$ to characterise the stability of the slugs.

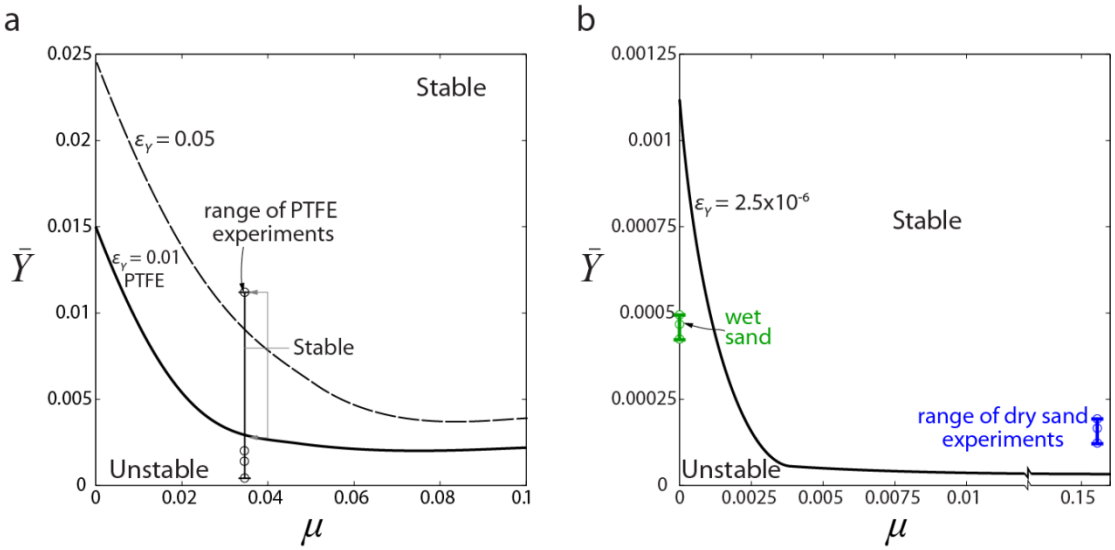

Figure 11: Stability maps in $\overline{Y}-\mu$ space for the slugs with Poisson's ratio $\nu = 0.49$,

[3] Over practical ranges of ρ_{slug}/ρ_0 for granular slugs subjected to air shocks in ambient air, the dependency of $\overline{Y}_c$ on ρ_{slug}/ρ_0 is very weak and hence for the sake of brevity we write $\overline{Y}_c(\varepsilon_c,\nu)$; see Section 5 for further details.

$A/\lambda = 0.01$, $D/\lambda = 3.5$ and $H/D = 1.4$. Results are shown for yield strains (a) $\varepsilon_Y = 1\%$ and 5% and (b) $\varepsilon_Y = 2.5 \times 10^{-6}$. The range of $\overline{Y}$ values investigated in this study for the PTFE slugs is marked in (a) and in (b) for the water-saturated and dry sand slugs. Each of the experiments listed in Table 2 is shown as a circle.

4.5 Stability maps for the three types of granular slugs

The stability maps in Fig. 10a demonstrate that the instability sets in when yield as given by the Drucker-Prager yield criterion is activated on the surface of the slugs. However, these maps are not useful to determine under what loading conditions a slug comprising a particular granular material becomes unstable as the demarking stable/unstable boundaries in Fig. 10a are themselves loading dependent. Stability maps again in $\overline{Y} - \mu$ space but with stable/unstable demarcation boundaries dependent only on material properties (and not on the loading) are more useful to examine the stability of granular slugs made from a given material, i.e. maps in $\overline{Y} - \mu$ space with the stable/unstable boundaries for a fixed ε_Y rather than a fixed $\hat{p}_r$. Calculations as described in Section 4.4 were performed by varying $\overline{Y}$ for combinations of (ε_Y,μ) with $\nu = 0.49$ to determine the minimum value $\overline{Y}_g$ to ensure a stable response, i.e. a stability criterion given as[4] $\overline{Y} \geq \overline{Y}_g(\nu,\varepsilon_Y,\mu)$ was determined. The stability maps obtained by such calculations are plotted in $\overline{Y} - \mu$ space in Fig. 11 for $\nu = 0.49$. In Fig. 11a we show the stable/unstable boundaries for $\varepsilon_Y = 0.05$ and 0.01 ($\varepsilon_Y = 0.01$ is representative of the PTFE sphere slug, see Table 1) while in Fig. 11b the boundary is plotted for $\varepsilon_Y = 2.5 \times 10^{-6}$ that is representative of the water-saturated and dry sand slugs. It is clear that increasing the yield strain increases the value of $\overline{Y}$ required to ensure a stable response while increasing the friction co-efficient stabilises the slug with stable responses obtained at lower values of $\overline{Y}$. These maps were computed using $\rho_{slug} = 2000$ kg m^{-3} (representative of water-saturated sand) but we emphasize that over the range of practical granular material densities, these boundaries are insensitive to the choice of ρ_{slug} (see Section 5 for further details).

Given that the maps in Fig. 11 are insensitive to ρ_{slug} we can use them to understand the experimental observations of the stable and unstable responses reported in Section 3. The ranges of experimental incident shock pressures are listed in Table 2 for the different granular slugs along with the stability of the observed response (i.e. stable or unstable). Using the properties of granular materials listed in Table 1, the bars in Figs. 11a and 11b show the range of experiments for the PTFE sphere slug and the water-saturated and dry sand slugs, respectively. Recall that the yield strain of the PTFE sphere slug is $\varepsilon_Y = 0.01$ and from Fig. 11a we see that the simulations predict that the experiments span both the stable and unstable regimes in line with observations. By contrast, the map in Fig. 11b shows that all experiments for the water-saturated sand fall within the unstable regime while all experiments of the dry sand fall within the stable regime, again consistent with observations. It can be concluded that the water-saturated sand was observed to have an unstable response primarily due to its low friction co-efficient compared to the dry sand while the PTFE

[4] As mentioned earlier, the function $\overline{Y}_g(\nu,\varepsilon_Y,\mu)$ can also be directly inferred from $\overline{Y}_c(\varepsilon_c,\nu)$ presented in Fig. 10b; see Appendix B for details.

slug was unstable at relatively low shock pressures (even though it had a high friction co-efficient) due to its high yield strain. We note in passing that for the water-saturated and dry sand, the stable/unstable boundary is insensitive to μ for $\mu \geq 0.005$. Thus, we do not expect any inaccuracy in estimating φ from cone angle tests to result in any change to the main conclusions drawn here.

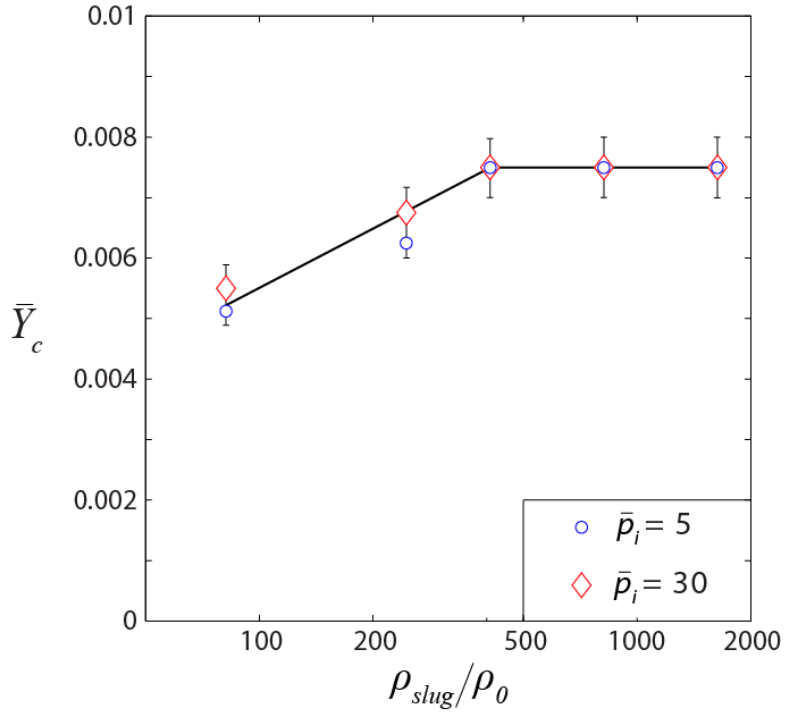

Figure 12: Predictions of $\overline{Y}_c$ as a function of the normalised slug density ρ_{slug}/ρ_0 for frictionless ($\mu = 0$) slugs with $\varepsilon_Y = 0.1\%$, $\nu = 0.49$, $A/\lambda = 0.01$, $D/\lambda = 3.5$ and $H/D = 1.4$. Results are shown for shock loads $\overline{p}_i = 5$ and 30 propagating through air under STP conditions.

5. Instabilities in pressure loaded granular slugs

The fluid/solid interaction simulations reported above successfully reproduce the main experimental observations regarding the establishment of the instability as a function of material properties and loading conditions. In this section we aim to understand the physical origins of the instability including the role of the fluid/solid interactions. Unless otherwise specified, all calculations in this section are reported with a Poisson's ratio $\nu = 0.49$ and consistent with the parameters used in the comparisons with experiments we fix $D/\lambda = 3.5$ and $H/D = 1.4$. Moreover, recall that the stability criterion is fully characterised by the function $\overline{Y}_c(\varepsilon_Y,\nu)$. Hence, in this section we report calculations for the frictionless solid ($\mu = 0$) which, given the plastic flow rule (4.2), is equivalent to a standard J_2 flow theory solid. The predictions of $\overline{Y}_c(\varepsilon_Y,\nu)$ can be used to infer $\overline{Y}_g(\varepsilon_Y,\nu,\mu)$ via the prescription in Appendix B (also see Section 4.4).

5.1 Influence of the Atwood number

The instability observed in the granular materials is reminiscent of the Richtmyer-Meshkov instability (RMI) (Richtmyer, 1960) that develops at the interface of two (*inviscid and zero shear strength*) fluids due to the passage of a shock wave. The growth of Richtmyer-Meshkov instabilities is strongly dependent on the density ratio

of the two fluids as parameterised by the Atwood number. In the case of granular slugs loaded by air shock waves, the Atwood number can be written in terms of the granular slug density ρ_{slug} and un-shocked air density ρ_0 as

$$\mathrm{A}_t \equiv \frac{\rho_{slug} - \rho_0}{\rho_{slug} + \rho_0}, \tag{5.1}$$

such that $0 \leq \mathrm{A}_t \leq 1$ since we restrict consideration to the practical limit wherein $\rho_{slug} \geq \rho_0$. Typically the growth rates of perturbations on the interface between the two fluids increases with increasing A_t due to larger differentials between the transmitted and reflected shock waves. In the case of most granular materials, $\rho_{slug} \gg \rho_0$ and it is unclear whether in this limit of $\mathrm{A}_t \rightarrow 1$, the Atwood number influences the onset of the instability.

Predictions of $\overline{Y}_c$ as a function of the normalised slug density ρ_{slug}/ρ_0 are presented in Fig. 12 for slugs with $A/\lambda = 0.01$, yield strain $\varepsilon_Y = 0.1\%$ and loadings $\overline{p}_i = 5$ and 30 (corresponding to $\overline{p}_r \approx 18$ and 200, respectively) via the passage of a shock through air at standard temperature and pressure (STP air). The error bars indicate the range over which $\overline{Y}_c$ is numerically determined. We observe that $\overline{Y}_c$ is independent of the slug density above $\rho_{slug}/\rho_0 \approx 400$: with the STP value of $\rho_0 = 1.22$ kg m^{-3}, this implies that the stability condition is independent of A_t for $\rho_{slug} \geq 500$ kg m^{-3}. Most practical granular materials fall in this range and thus for the purposes of granular materials loaded by air shocks the results of Fig. 12 suggest that it suffices to neglect the details of the fluid/solid interaction and model the loading of the slugs by directly imposing the reflected pressure p_r on the surface of the granular slug.

5.2 Equivalence of pressure loading and air shock loading

The direct pressure loading of the slugs can be modelled in a Lagrangian setting using the boundary value problem sketched in Fig. 13a. The sides of the slug are prevented from expanding with boundary conditions $u_2 = 0$ while traction free conditions are imposed on the free face of the slug at the distal end from the loaded face along with tractions $T_1 = 0$ on $x_2 = \pm D/2$. Similar to the Eulerian calculations, a geometrical imperfection in the form of a sinusoidal wave of amplitude A and wavelength λ is introduced on the loaded face and a spatially uniform pressure p_r imposed on this face at time $t_i = 0$. This pressure is introduced as a "follower" traction such that the resultant traction on this face has (compressive) magnitude p_r and is always normal to the surface (i.e. the resultant traction rotates along with the surface in the finite deformation Lagrangian analysis). The material properties in the Lagrangian analysis are identical to the Eulerian analysis, i.e. the solid is modelled as an isotropic elastic-plastic J_2 flow theory solid. All Lagrangian calculations were performed in the explicit time integration version of the commercial FE package ABAQUS using spatially uniform reduced integration four-noded plane strain quadrilaterals (CPE4R in ABAQUS notation) with 50 and 120 elements in the x_1 and x_2 – directions, respectively. We shall subsequently refer to the Eulerian calculations as fluid loading and the Lagrangian analysis as direct loading.

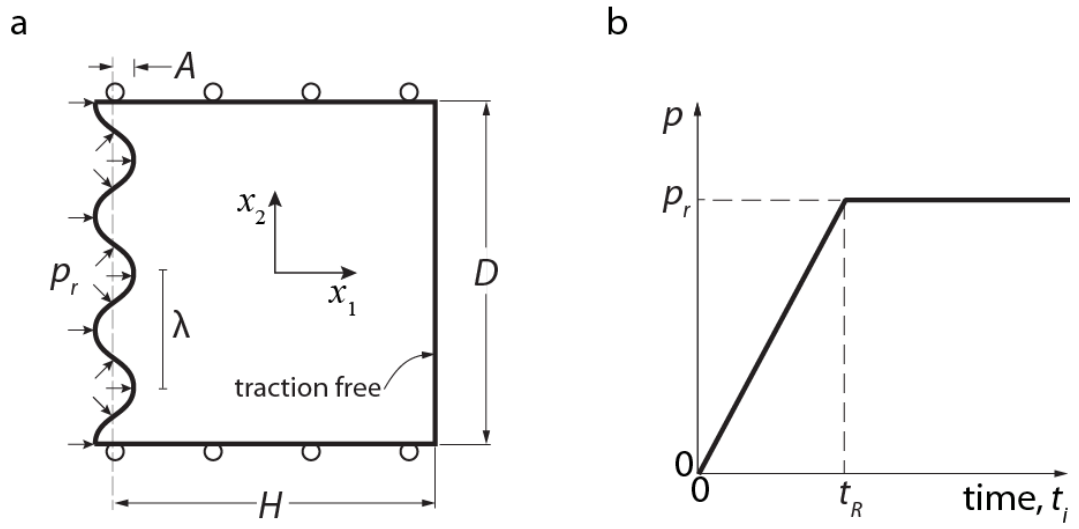

Figure 13: (a) Sketch of the direct pressure loading boundary value problem used in the Lagrangian calculations. (b) The temporal history of the applied pressure.

In order to compare the fluid loading and direct loading calculations we consider a slug with Young's modulus $E = 10$ MPa and yield strain $\varepsilon_Y = 0.1\%$, i.e. yield strength $Y = 0.01$ MPa. For the fluid loading case, loading is via shocks propagating through air initially under STP conditions and so the calculations have a fixed value of $p_0/E = 0.01$. A series of calculations were performed with increasing $\overline{p}_i$ in order to find the onset of the instability (using the criterion detailed in Section 4.4) and this critical incident shock pressure is denoted as p_i^c with p_r^c the corresponding reflected pressure that is related to p_i^c via Eq. (2.4). Predictions of $\overline{Y}_c \equiv Y/p_r^c$ are included in Fig. 14a as a function of the imperfection amplitude A/λ. An additional set of direct loading calculations with p_r directly imposed on the slug modelled in the Lagrangian setting were also performed and predictions of $\overline{Y}_c$ via this method also included in Fig. 14a. Excellent agreement is observed between the two types of calculations confirming that the onset of the instability is adequately captured by directly imposing the reflected pressure due to air shock loading without explicitly modelling the fluid/solid interaction.

While direct loading is adequate to capture the onset of the instability, we emphasize that the evolution is strongly dependent on the fluid/solid interaction. To demonstrate this we define $\Delta A_{\max}(t_i) \equiv \max\left[\left|h(x_2,t_i) - H\right|\right] - A$, where $t_i = 0$ corresponds to the instant the shock impinges on the slug in the fluid loading case and when the pressure was imposed for the directly loading case while $h(x_2,t_i)$ is the length of the slug at ordinate x_2. Predictions of the evolution of $\Delta A_{\max}/\lambda$ with $t_i c_L/\lambda$ are included in Fig. 14b ($A/\lambda = 0.01$) for the both the fluid and direct loading cases with $\hat{p}_r = 0.20$ and 0.10. The $\hat{p}_r = 0.10$ case results in a stable response with no growth in $\Delta A_{\max}$ while with $\hat{p}_r = 0.20$ there is a runaway growth in $\Delta A_{\max}$ corresponding to an unstable response for both the fluid and direct loading cases. However, the growth of $\Delta A_{\max}$ is

faster in the direct loading case. This is because a temporally constant pressure p_r is imposed in that case while the motion of the slug reduces the reflected shock pressures in the fluid loading case which in turn decreases the growth rate of the imperfections. This is further illustrated in Fig. 14c, where we include predictions of the spatial distributions of the normalised pressure $-\sigma_{kk}/(3E)$ for $\hat{p} = 0.20$ at selected times $t_i c_L/\lambda$. Here the differences in the evolution of the slug geometry between the direct and fluid loading cases are more clearly seen. In fact, differences in the surface profile evolutions also result in differences in the pressure distributions within the slug.

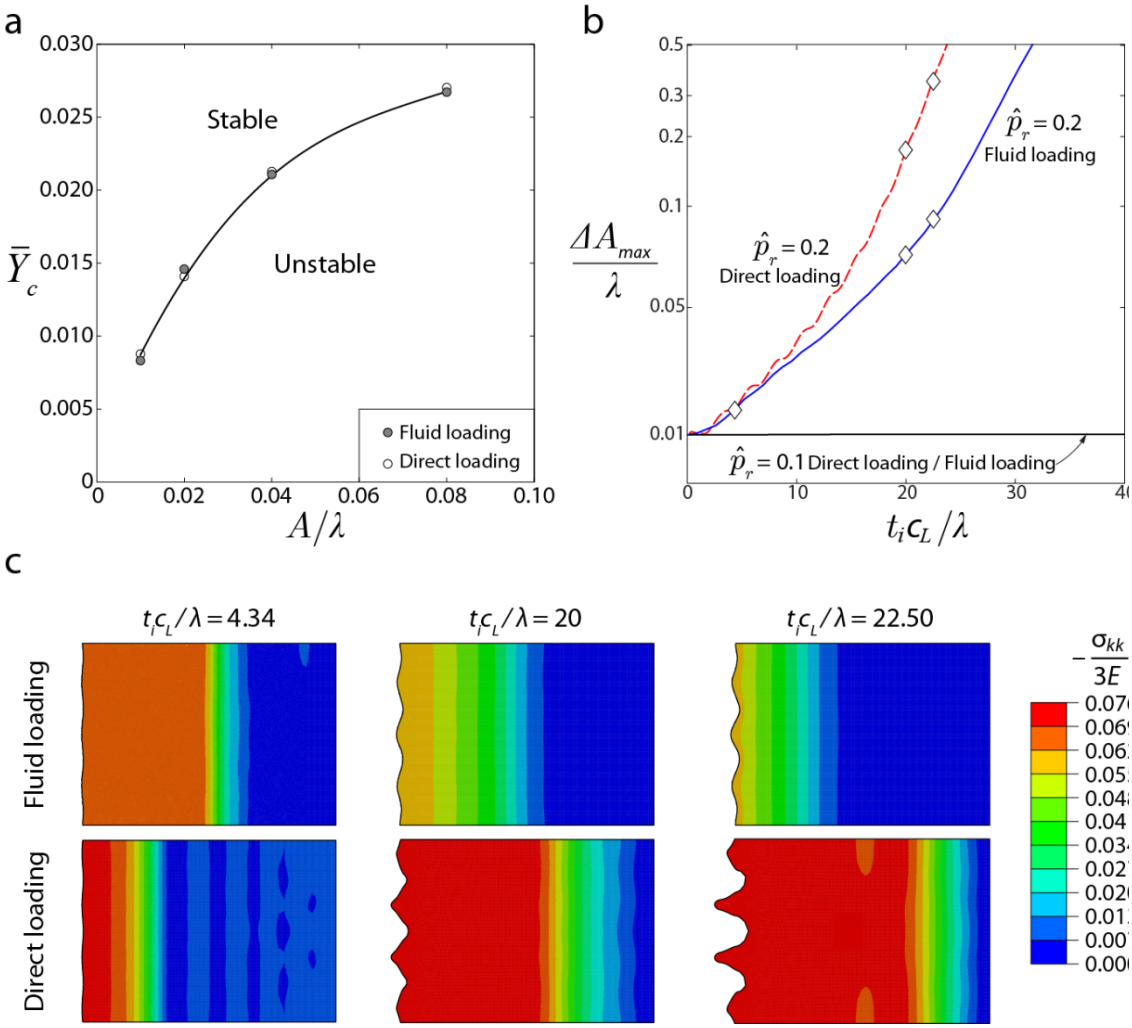

Figure 14: Comparison of the fluid loading and direct loading predictions for the frictionless slug with $E = 10$MPa, $\nu = 0.49$, $\varepsilon_Y = 0.1\%$, $D/\lambda = 3.5$ and $H/D = 1.4$. (a) Predictions of $\bar{Y}_c$ as a function of A/λ. (b) Fluid and direct loading predictions of the temporal evolution of $\Delta A_{\max}/\lambda$ in the slug with $A/\lambda = 0.01$ for applied loadings $\hat{p}_r = 0.10$ and 0.20. (c) Evolution of the slug geometry of the direct and fluid loaded slug in (b) with $\hat{p}_r = 0.20$. The slug is shown at three selected times with spatial distributions of the normalised pressure $-\sigma_{kk}/(3E)$. Here time $t_i = 0$ corresponds to the instant the shock wave from the fluid impinges on the slug or the direct loading is initiated.

5.3 Physical origins of the instability

The direct loading problem is inherently simpler to interpret, as deformation/flow in the fluid is not included in the analysis. Given the equivalence between fluid and direct loading for predicting the onset of the instability, we use direct loading calculations to examine the origins of the instability.

To develop a better understanding of the shock loading effects, consider a spatially uniform imposed pressure p that has the temporal variation sketched in Fig. 13b: p is increased linearly with time from time $t_i = 0$ until it reaches a plateau value, p_r at $t_i = t_R$ with $p = p_r$ for $t_i \geq t_R$. Thus, as $t_R c_L/H \to 0$ the shock-loading limit is attained (reminiscent of the RMI) while we might expect to attain the Rayleigh-Taylor (Taylor, 1950) limit of a slug subjected to an acceleration $p_r/(\rho_{slug} H)$ as $t_R c_L/H \to \infty$. This simple temporal pressure history is imposed in order to aid the understanding of effect of loading rate: full fluid/solid interactions with the consequent complex loading histories have been analysed in Section 4. In the calculations that follow, $\varepsilon_Y = 0.1\%$ and $A/\lambda = 0.01$.

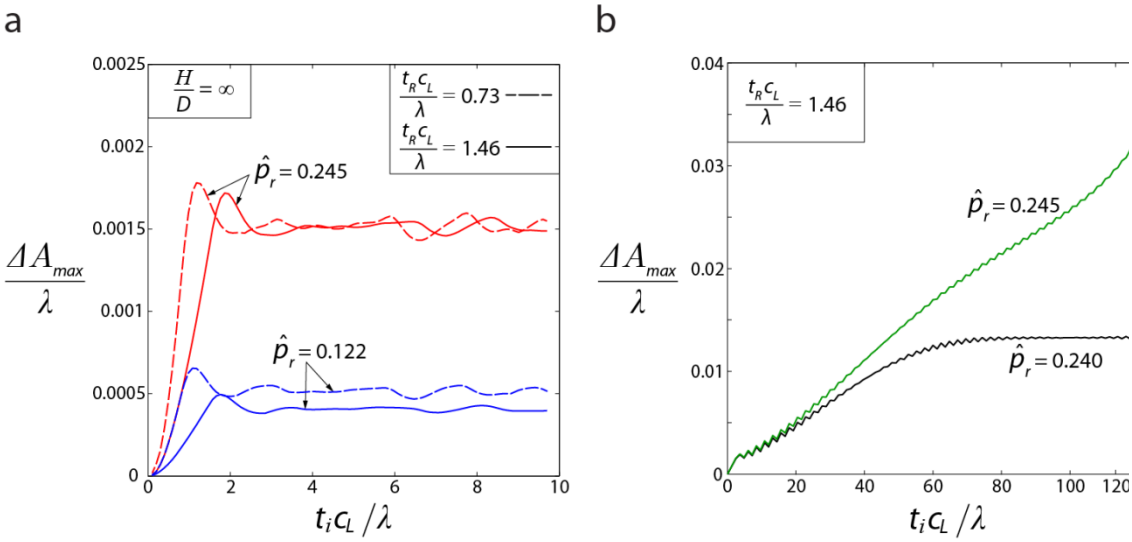

Figure 15: Predictions of the temporal evolution of the surface perturbation of the directly loaded frictionless slugs with $\nu = 0.49$, $\varepsilon_Y = 0.1\%$, $A/\lambda = 0.01$ and $D/\lambda = 3.5$. Results are shown for (a) an infinitely long slug ($H/D = \infty$) and (b) a $H/D = 1.4$ slug. In each case predictions are shown for selected values of the normalised pressure $\hat{p}_r$ and ramp time $t_R c_L/\lambda$ as indicated. Here time $t_i = 0$ corresponds to the instant direct loading is initiated.

First consider the case of an infinitely long slug such that $H/D \to \infty$ with all other parameters fixed at their reference values. Predictions of the temporal evolution of $\Delta A_{\max}$ for $\hat{p}_r \equiv p_r/E = 0.122$ and 0.245 are included in Fig. 15a for two values of the non-dimensional rise time $t_R c_L/\lambda$ in each case. In all cases $\Delta A_{\max}$ increases over the time range $0 \leq t_i \leq t_R$ and then plateaus out. The plateau value of $\Delta A_{\max}$ increases with increasing $\hat{p}_r$ but is less sensitive to $t_R c_L/\lambda$. In fact, irrespective of the applied $\hat{p}_r$, a runaway increase in $\Delta A_{\max}$ such as seen in Fig. 14b, was never observed suggesting that the infinitely long slugs are always stable when subjected to pressure loading. Now consider the case of a finite slug with $H/D = 1.4$ and $t_R c_L/\lambda = 1.46$.

Predictions of the temporal evolution of $\Delta A_{\max}$ were included in Fig. 15b for two values of $\hat{p}_r$ on either side of the critical pressure required to cause the unstable deformation of the slug. For $\hat{p}_r = 0.24$, $\Delta A_{\max}$ plateaus out at $\Delta A_{\max}/\lambda \approx 0.015$ suggesting that the slug remains stable when subjected to this level of imposed pressure. However, $\Delta A_{\max}$ clearly continues to increase resulting in an unstable response for the $\hat{p}_r = 0.245$ case. We note that with $\hat{p}_r = 0.245$, $\Delta A_{\max}/\lambda$ plateaued at ≈ 0.0015 for the $H/D \to \infty$ slug suggesting that the decrease in H/D has initiated the instability. Moreover, $\Delta A_{\max}/\lambda$ in Fig. 15b increases in a staircase manner with a step time that is $\sim H/c_L$. This suggests that wave reflections from the distal free surface of finite length slugs play an important role.

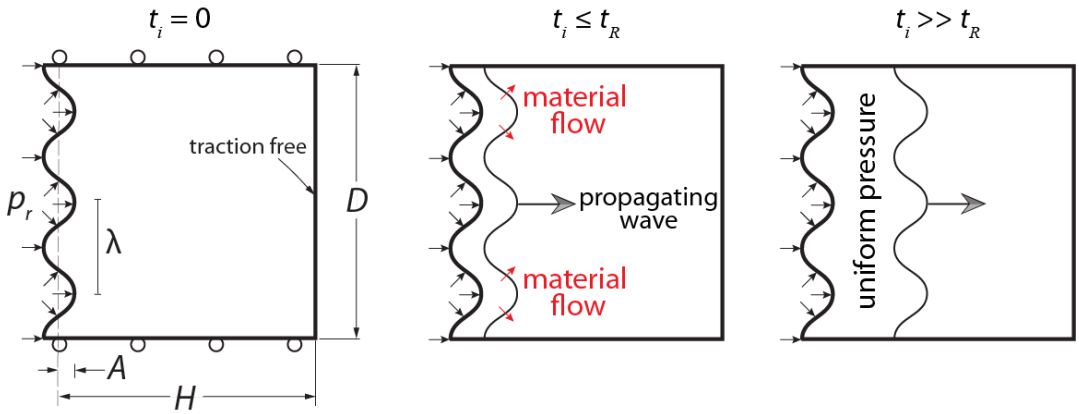

Figure 16: Sketch showing the wave propagation into a slug due to pressure loading on its wavy surface. The wavy wave front results in a spatial pressure gradient that can cause material flow as indicated.

These results give insight into the deformation modes that result in stable or unstable responses. To understand their significance, consider the sketch of the slug in Fig. 16 with a sinusoidally perturbed surface loaded by a pressure p having the temporal distribution shown in Fig. 13b. The shock wave emanating from this loading traverses through the slug towards the traction free distal face of the slug and the position of the wave at some time $t_i \le t_R$ is shown in Fig. 16. The wavefront has the wavy character inherited from the initial waviness of the loaded surface. This implies that there is a spatial pressure gradient near the wave front that can cause plastic flow of the material as indicated in Fig. 16 (provided the pressure and hence the gradients are sufficiently high to cause plastic deformations). For $t_i \gg t_R$, the pressure is spatially uniform with a value p_r behind the wavefront while the slug remains unloaded ahead of the wave. Thus, as the wave traverses away from the loaded surface, the deformation at a fixed location will cease. In the limit $H \to \infty$ slug, spatial pressure gradients near the surface are only present over the time period $0 \le t_i \le t_R$ and hence $\Delta A_{\max}$ in such slugs grows only over that period. In the finite length slugs, the wavy wave front reaches the distal free surface and reflects. These reflections carry perturbations associated with the initial wavy wave front and deposit spatial fluctuations in the pressure field near loaded surface. Continued increase in $\Delta A_{\max}$ occurs with each reflection resulting the staircase growth of $\Delta A_{\max}$ seen in Fig. 15b.

Unstable growth in the waviness of the surface sets in once $\Delta A_{\max}$ reaches some critical threshold. Thus, just like the Rayleigh-Taylor (Taylor, 1950) and Richtmyer-Meshov (Richtmyer, 1960) instabilities, the instabilities investigated here are driven by spatial pressure gradients. We thus argue that the phenomenon investigated here requires some form of initial imperfection. In fact the computational predictions in Fig. 14a suggest that $\overline{Y}_c \to 0$ in the limit $A/\lambda \to 0$ suggesting that the unstable growth is not a bifurcation phenomenon but an outcome of the growth of an initial imperfection as in the Rayleigh-Taylor or Richtmyer-Meshov instabilities.

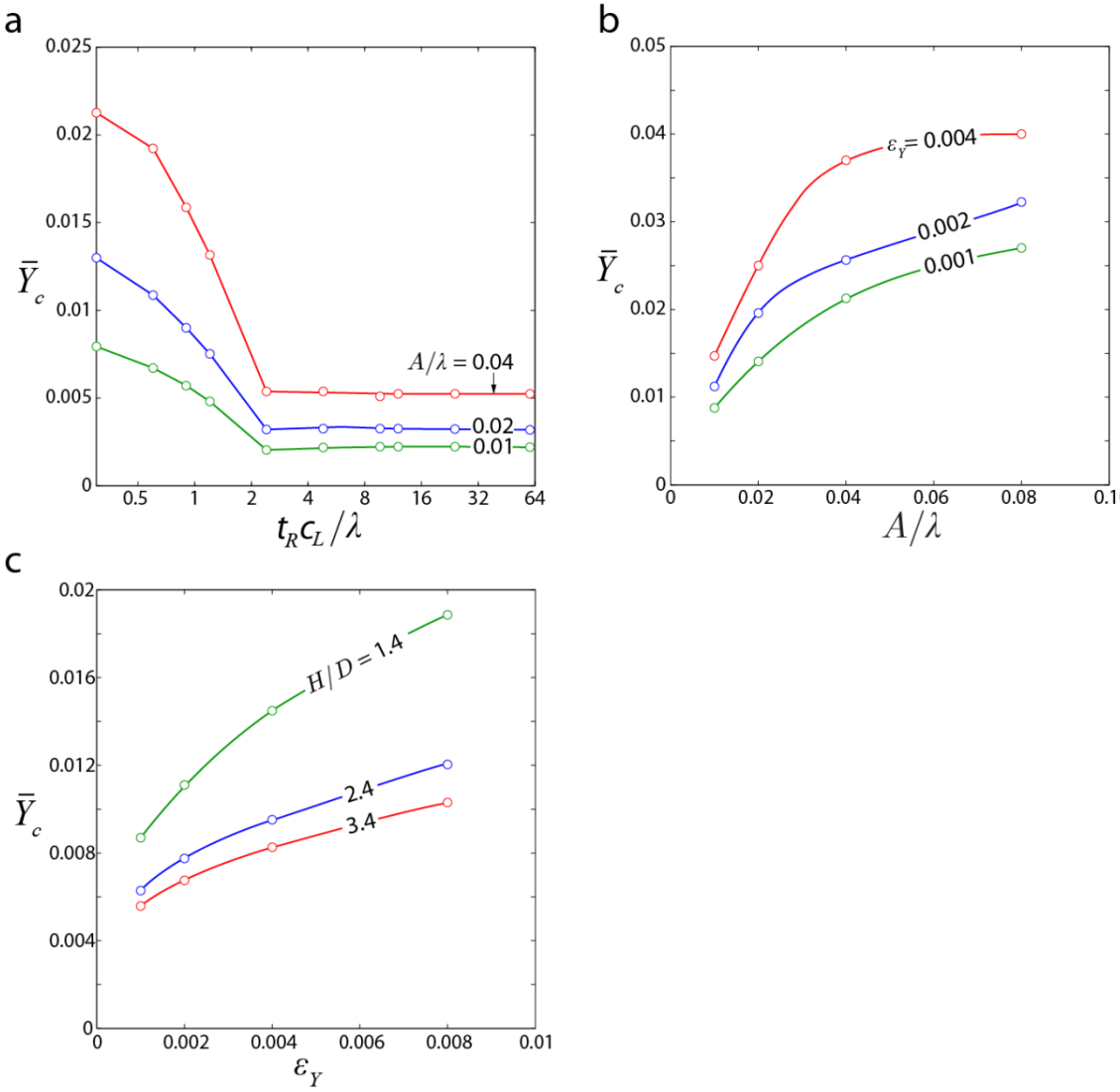

Figure 17: Parametric dependency of the stability condition with reference parameters $\nu = 0.49$, $\varepsilon_Y = 0.1\%$, $A/\lambda = 0.01$, $D/\lambda = 3.5$, $H/D = 1.4$ and ramp time $t_R c_L/\lambda = 0$. Predictions of the dependence of $\overline{Y}_c$ (a) on $t_R c_L/\lambda$ for selected values of A/λ, (b) on A/λ for selected values of ε_Y and (c) on ε_Y for selected values of H/D.

5.4 Influence of material, geometric and loading parameters

To explore the sensitivity of the stability condition to loading, material and geometrical parameters, a parametric study of each variable (while keeping the other parameters held fixed at their reference value) is conducted. The reference conditions are taken to be $H/D = 1.4$, $A/\lambda = 0.01$, $\varepsilon_Y = 0.1\%$ and ramp time of the loading $t_R c_L$

$/\lambda = 0$. The loading is via the directly applied pressure p with a temporal variation as shown in Fig. 13b. Results are reported in terms of the minimum normalised yield strength $\overline{Y}_c \equiv (Y/p_r)_{\text{crit}}$ for a stable response with stability defined by the criterion given in Section 4.4.

Predictions of the variation of $\overline{Y}_c$ for stability with rise time $t_R c_L/\lambda$ for selected values of A/λ are shown in Fig. 17a. The critical strength $\overline{Y}_c$ first decreases with increasing $t_R c_L/\lambda$ and then plateaus out and increases with increasing A/λ. Shock loading corresponding to small $t_R c_L/\lambda$ cause large gradients in the pressure early in the loading history ($t_i < t_R$) leading to an increase in $\Delta A_{\max}$ which in turn requires a higher yield strength to enforce stability. Similarly, a large initial imperfection increases the spatial pressure gradients thereby increasing $\overline{Y}_c$.

The effect of the initial waviness amplitude A/λ at $t_R c_L/\lambda = 0$ is summarised in Fig. 17b for three values of ε_Y. The critical strength $\overline{Y}_c$ increases with both increasing A/λ and ε_Y. The increase with ε_Y is understood by noting that the elastic deformations increase with increasing yield strain ε_Y and a larger yield strength is then required to inhibit unstable growth of the surface perturbations. All results discussed in the context of Fig. 17 have so far been restricted to slugs of aspect ratio $H/D = 1.4$. It is observed in Fig. 17c that $\overline{Y}_c$ decreases with increasing H/D, consistent with the discussion in Section 5.3 that showed $\overline{Y}_c \to 0$ in the limit $H/D \to \infty$.

5.5 Relation to the Rayleigh-Taylor instability

The problem under discussion here, namely instabilities in a solid accelerated by a pressure, is reminiscent of the widely investigated Rayleigh-Taylor instability (RTI). While most investigations of RTI have focussed on fluids, there exists a small literature on RTI solids starting with the pioneering work of Drucker (1980) for rigid-plastic solids. This has been subsequently extended to elastic-plastic solids; see for example Piriz et al. (2009). Importantly, analytical expressions for the stability criterion have been derived in the limit of an incompressible elastic-plastic solid (i.e. $\nu = 0.5$). It is instructive to compare the numerical calculations of Section 5.4 with these analytical predictions.

In the calculations in Section 5.4, results were presented that spanned from the shock loading limit $t_R c_L/\lambda = 0$ to $t_R c_L/\lambda \to \infty$. The shock loading limit, corresponds to the problem analysed by Richtmyer (1960) for an ideal inviscid fluid and in this limit there are no analytical treatments for elastic-plastic solids. However, the $t_R c_L/\lambda \to \infty$ limit might be expected to represent the Rayleigh-Taylor problem that can be stated as follows. A *geometrically perfect* slug of height H is accelerated from time $t_i = -\infty$ to $t_i = 0$ by a pressure p_r such that at $t_i = 0$ it is accelerating like a rigid body with acceleration $p_r/(\rho_{slug} H)$. At time $t_i = 0^+$, the geometrical imperfection as sketched in Fig. 13a is suddenly introduced on the loaded surface (or alternatively a spatial perturbation introduced into the applied pressure). Piriz et al. (2009) showed that the critical yield strength $\overline{Y}_c$ of the incompressible solid in such circumstances is given by

$$\frac{1}{\sqrt{3\overline{Y}_c}}\left(\frac{A}{H}\right) = 1 - \sqrt{\frac{3\varepsilon_Y}{4\pi\overline{Y}_c}\left(\frac{\lambda}{H}\right)}, \tag{5.2}$$

where the solution $\overline{Y}_c$ corresponds to the root of Eq. (5.2) that that satisfies the conditions

$$\frac{1}{\sqrt{3\overline{Y}_c}}\left(\frac{A}{H}\right) \leq 1 \quad \text{and} \quad \frac{3\varepsilon_Y}{4\pi\overline{Y}_c}\left(\frac{\lambda}{H}\right) \leq 1. \tag{5.3}$$

Finite element predictions of $\overline{Y}_c$ as a function of A/λ are included in Fig. 18 for the reference values of $H/D = 1.4$ and $D/\lambda = 3.5$ and two choices of the yield strain $\varepsilon_Y = 0.1\%$ and 1%. These numerical calculations were performed with the choice $t_R c_L/\lambda = 50$ as no differences in $\overline{Y}_c$ were observed by further increasing $t_R c_L/\lambda$ (Fig. 17a). The analytical predictions given by Eqs. (5.2) and (5.3) are also included in Fig. 18. The analytical predictions significantly underestimate $\overline{Y}_c$ for $\varepsilon_Y = 1\%$ and for the lower values of A/λ in the $\varepsilon_Y = 0.1\%$ case. In fact there seems little direct correlation between the two sets of predictions. This discrepancy can be understood by recalling that in the analytical calculations, the slug was loaded with a pressure p_r and has a sinusoidal imperfection with amplitude A and wavelength λ, at time $t_i = 0^+$. By contrast, in the numerical calculations, the applied pressure attained a value p_r at $t_i c_L/\lambda = 50$ by which time the surface imperfections had grown due to gradients associated with the pressure ramp. Higher yield strengths are then needed to stabilise slugs with these enlarged imperfections in the numerical calculations. It can be concluded that the analytical RTI predictions that model solids subject to constant acceleration (and neglect wave effects) cannot be used to predict the stability of pressure loaded granular slugs, even in the non-shock limit of $t_R c_L/\lambda \to \infty$.

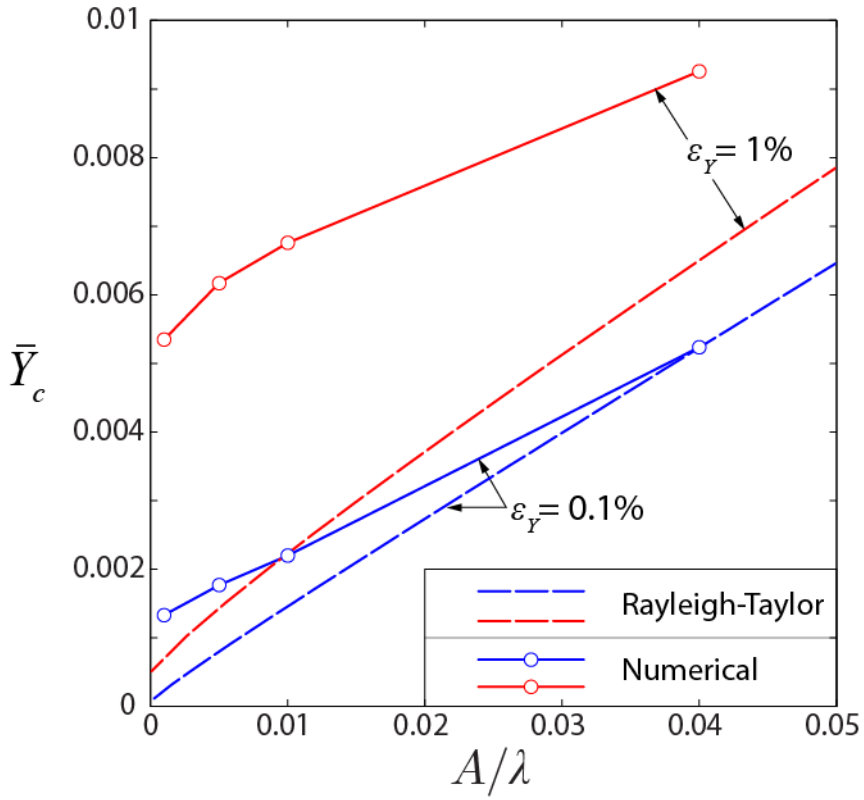

Figure 18: Comparison of direct loading and analytical Rayleigh-Taylor predictions of the variation of $\bar{Y}_c$ with A/λ for frictionless slugs with $\varepsilon_Y = 0.1\%$ and 1%. The numerical predictions were conducted with the parameters $\nu = 0.49$, $D/\lambda = 3.5$, $H/D = 1.4$ and ramp time $t_R c_L/\lambda = 50$.

6. Dynamic pressure loading of rear-supported granular slugs

The instability in the free-standing slug was shown above to arise from reflections of waves carrying perturbations due to the initial geometrical imperfections on the loaded surface. Thus, there seems, a-priori, no reason for instabilities to exist only in free-standing slugs. Here we investigate instabilities in rear-supported slugs to explore if surface instabilities can occur due to reflections from a fixed distal slug surface.

6.1 Observations of instabilities in rear-supported PTFE sphere slugs

The experiments of Section 3 demonstrated that current experimental set-up was able to induce both stable and unstable responses in the PTFE sphere slugs, i.e. these slugs are the most versatile from an experimental standpoint. Thus, for the rear-supported slug experiments reported here we restrict attention to the PTFE sphere slugs.

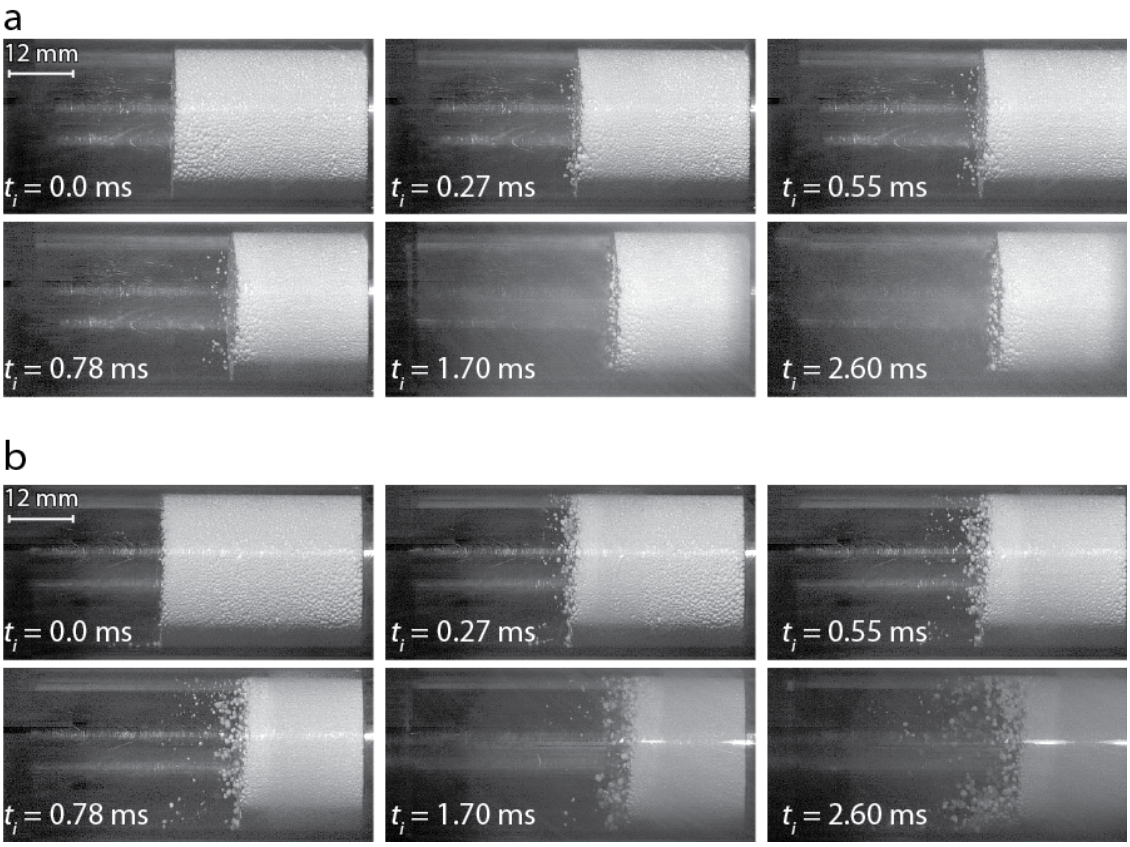

Figure 19: Montage of high-speed photographs showing the evolution of the rear-supported PTFE sphere slugs loaded by a (a) $\overline{p}_i = 4.1$ ($P_c = 1.6$ MPa) and (b) $\overline{p}_i = 5.9$ ($P_c = 7.3$ MPa) shock wave. Here time $t_i = 0$ corresponds to the instant the incoming shock first impinges on the surface of the slug.

PTFE sphere slugs were prepared as detailed in Section 2.1 but the PC tube in which the slugs were constrained was capped on the rear face of the slug as shown in Fig. 3a. Again the PC tube was attached to the pressure apparatus such that the free-face of the slug was 85 mm from the pressure sensor and shock loading experiments conducted as described in Section 2. High-speed photographs of the deformation of PTFE sphere slugs loaded by shocks initiated with cylinder pressures $P_c = 1.6$ MPa and 7.3 MPa are shown in Figs. 19a and 19b, respectively (in total, three values of P_c investigated here as detailed in Table 2). These cylinder pressures generate incoming shock pressures $\overline{p}_i = 4.1$ and 5.9, respectively (as measured by the pressure sensor) and time $t_i = 0$ in Fig. 19 corresponds to the instant that the incoming shock first impinges on the PTFE sphere slug. For both the pressure loadings, the slug undergoes significant compression but no surface instability is observed in the $\overline{p}_i = 4.1$ case. On the other hand, with $\overline{p}_i = 5.9$ a weak surface instability develops with PTFE spheres seen coming off the surface. We emphasize that this is not due to an elastic rebound of the slug as the reflected pressure is approximately constant over the duration of the images shown in Fig. 19 (consistent with the fact that there is no overall recovery of the compressive elastic deformation of the slug).

6.2 Simulations of instabilities in rear-supported slugs

The stability of the slugs can be investigated by performing direct pressure loading Lagrangian calculations using a J_2 flow theory solid as discussed previously. Thus, in order to investigate the stability of the rear-supported slugs this methodology was used to analyse the boundary value problem sketched in Fig. 20a. Results are reported for the reference case with $\nu = 0.49$, $H/D = 1.4$, $D/\lambda = 3.5$ and $A/\lambda = 0.01$. Attention is restricted to the shock loading limit with $t_R c_L/\lambda = 0$ so a spatially and temporally constant pressure p_r can be applied for time $t_i \geq 0$.

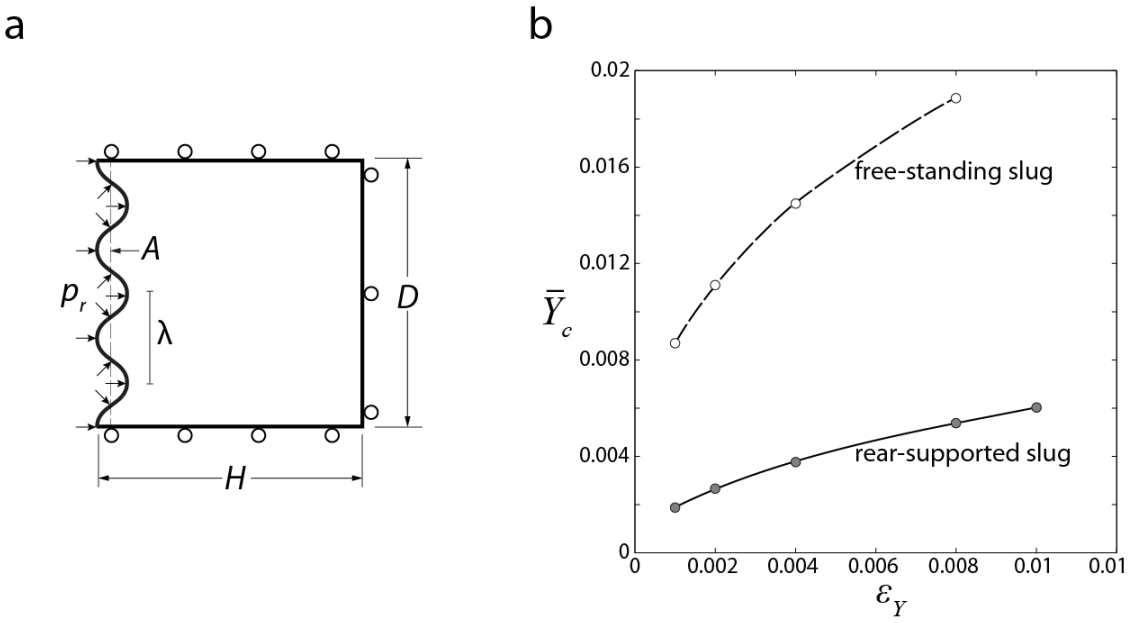

Figure 20: (a) Sketch of the direct loading boundary value problem for investigating the response of shock loaded rear-supported slugs. (b) Predictions of the variation of $\overline{Y}_c$ with yield strain ε_Y for rear-supported frictionless slugs with $\nu = 0.49$, $H/D = 1.4$, $D/\lambda = 3.5$, $A/\lambda = 0.01$ and loaded with $t_R = 0$. The corresponding results for the free-standing slug from Fig. 17c are also included.

Predictions of $\overline{Y}_c$ as a function of ε_Y are included in Fig. 20b. Similar to the equivalent free-standing results in Fig. 17c, $\overline{Y}_c$ increases with increasing ε_Y but $\overline{Y}_c$ required to ensure stability of the rear-supported slugs is significantly lower than that for a free-standing slug made from a material with the same yield strain (see Fig. 20b). It can be concluded that while surface instabilities can occur in rear-supported slugs, higher shock pressures are required compared to otherwise identical free-standing slugs.

6.3 Stability map for rear-supported PTFE sphere slugs

It is instructive to develop stability maps for the rear-supported PTFE slugs similar to those of Fig. 11 for the free-standing slugs. The stability map with axes $\overline{Y}$ and μ was constructed from the data in Fig. 20b and using the prescription outlined in Appendix B. Such a map for $\varepsilon_Y = 0.01$ (representative of the PTFE sphere slug; Table 1) is plotted in Fig. 21 and the corresponding demarking boundary from Fig. 11a, for free-standing PTFE sphere slugs, is also included. As anticipated, for all values of μ, the rear-supported PTFE sphere slug remains stable to lower values of $\overline{Y}$ compared to the free-standing slug.

Experiments showing stable and unstable behaviour were reported in Section 6.1 and listed in Table 2. The location of these experiments is included on the map in Fig. 21, by using the reflected pressures calculated from Eq. (2.4) along with the yield strength Y and friction co-efficient μ of the PTFE sphere slug from Table 1. In line with observations, the simulations indicate that the slug loaded with $\overline{p}_i = 4.1$ remains stable while loading with the higher pressures $\overline{p}_i = 5.5$ and 5.9 results in an unstable response.

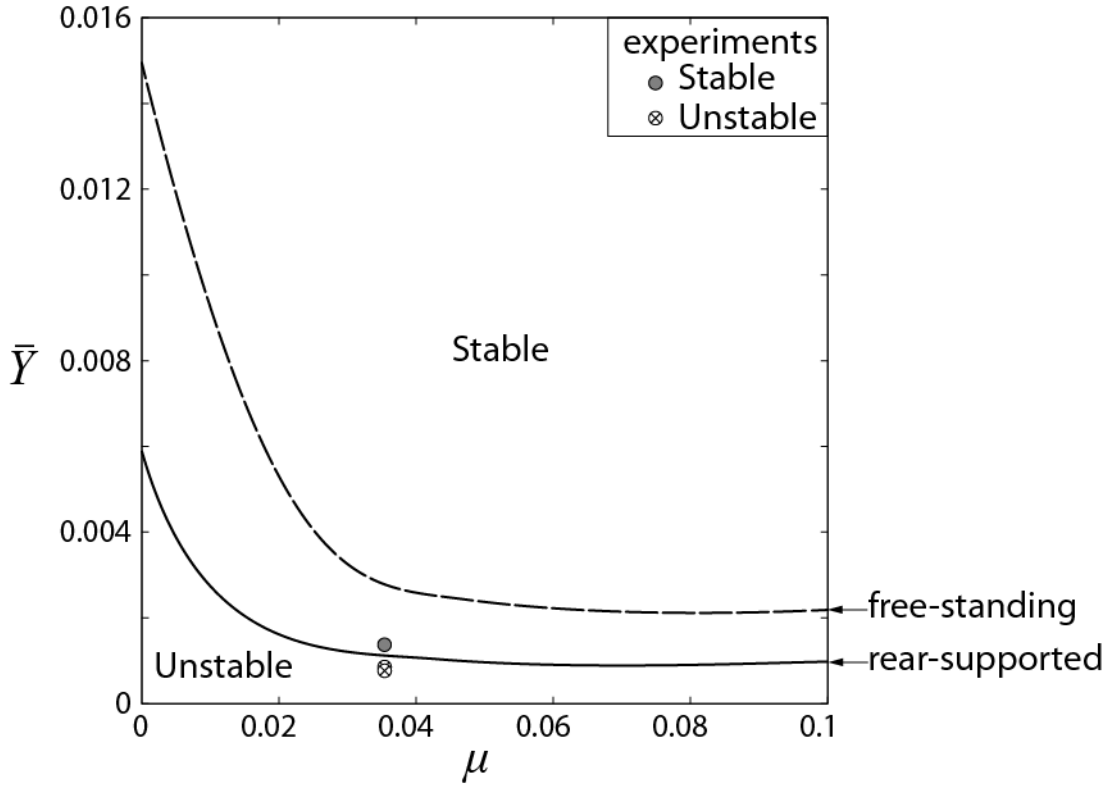

Figure 21: Stability map for the rear-supported PTFE slug ($\varepsilon_Y = 0.01$) in $\overline{Y} - \mu$ space. The corresponding demarcation boundary between stable and unstable responses for the free-standing PTFE slug from Fig. 11a is included for comparison purposes. The locations of the three rear-supported experiments (Table 2) are indicated on the map.

7. Surface instabilities on the front face of accelerated granular slugs

Recall that instabilities are observed on both sides of a granular shell accelerated by explosive gases, i.e. the side exposed to the high-pressure explosive gases as well as the side in contact with atmospheric air (Fig. 1). The experiments and simulations reported so far in this study suggest that instabilities only develop on the surface loaded by a high-pressure incoming shock and not on the surface of the slug exposed to atmospheric air (referred to here as the front face). In this section we investigate whether instabilities can arise on the front face via the mechanisms discussed above and if this is so, what is the criterion that leads to the initiation of these instabilities.

7.1 Simulations of front face instabilities

Eulerian coupled fluid/solid loading simulations were conducted for shock loading of the PTFE sphere slug by an incoming shock pressure $\overline{p}_i = 30$. These shock tube simulations were conducted as described in Section 4 with the PTFE sphere slug properties listed in Table 1 and the geometrical parameters from Section 4.2. Snapshots showing the predictions evolution of the slug with time t_i are included in Fig. 22 with $t_i = 0$ corresponding to the instant that the incoming shock wave impinged on the slug. The growth of surface perturbations on the surface of the slug impinged by the incoming shock wave are clearly at $t_i = 0.4$ ms. At this point the front face perturbations had grown substantially less. However, by $t_i = 0.85$ ms large growth in surface perturbations (i.e. instabilities) are seen on both faces of the slug resulting in mixing of the slug with air on both surfaces. This is in contrast to the corresponding results for $\overline{p}_i = 4.2$ shown in Fig. 9b where only surface perturbations on the surface impinged by the shock wave were observed to grow even at $t_i = 3.4$ ms.

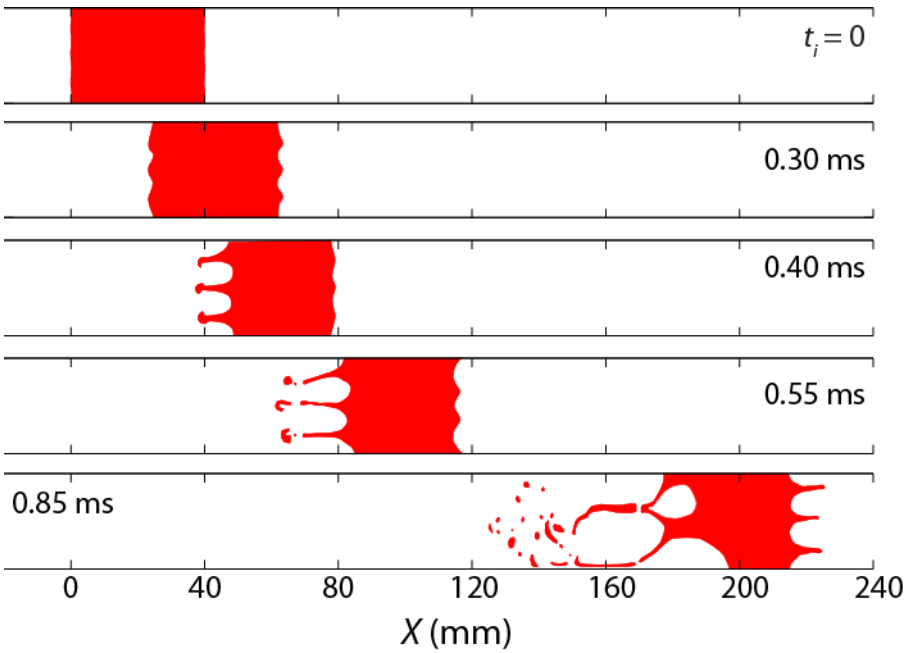

Figure 22: Snapshots of the evolution of the slug shape from Eulerian simulations of the PTFE sphere slug loaded by an incoming normal shock of magnitude $\overline{p}_i = 30$. Here time $t_i = 0$ corresponds to the instant the incoming shock first impinges on the surface of the slug.

To understand the instabilities on the front face of the slug, consider the one-dimensional case of a slug moving with a velocity V_s into STP air. The slug generates a shock wave as it pushes into the STP air. Assuming that the slug attains the velocity V_s impulsively[5], the shock pressure p_f at the front of the slug is related to V_s via (Liepmann and Roshko, 2001)

[5] Even if the slug attains the velocity V_s gradually rather than impulsively, the uniform state behind the shock described here, is eventually attained since non-uniformities in the compressed region catch up with the shock front.

$$\frac{V_s}{a_0} = \frac{1}{\gamma}(\bar{p}_f - 1)\left[\frac{2\gamma}{\bar{p}_f(\gamma+1)+\gamma-1}\right]^{1/2}, \tag{7.1}$$

where $\bar{p}_f \equiv p_f/p_0$ and the shock speed c_f is given by

$$\frac{c_f}{a_0} = \left[\frac{\gamma-1}{2\gamma} + \bar{p}_f\frac{\gamma+1}{2\gamma}\right]^{1/2}. \tag{7.2}$$

Thus, with increasing V_s, $\bar{p}_f$ increases resulting in a larger pressure being exerted on the front face of the slug. This front face pressure loading results in the front face instability similar to pressure loading due to the incoming shock creating an instability on the face of the slug impinged by the incoming shock.

The key difference between the simulations of Figs. 9b and 22 is the shock pressure $\bar{p}_i$. The significantly higher shock loading pressure in Fig. 22 results in the slug acquiring a significantly higher velocity: a comparison of Figs. 9b and 22 reveals that at time $t_i \approx 1$ ms, the front face of the slug had travelled ~210 mm when loaded with $\bar{p}_i = 30$ compared to ~ 20 mm when loaded with $\bar{p}_i = 4.2$. This higher slug velocity causes larger front pressures p_f to develop that trigger instabilities on the front face of the slug loaded with $\bar{p}_i = 30$. In the experiments performed in this study, the shock loading pressures are relatively low (constrained by the bursting pressure of the PC tube) and hence the slug velocities were also insufficient to initiate strong shocks on the slug front surfaces. Thus, front face instabilities were not observed in either the experiments or the low shock pressure simulations reported in earlier sections.

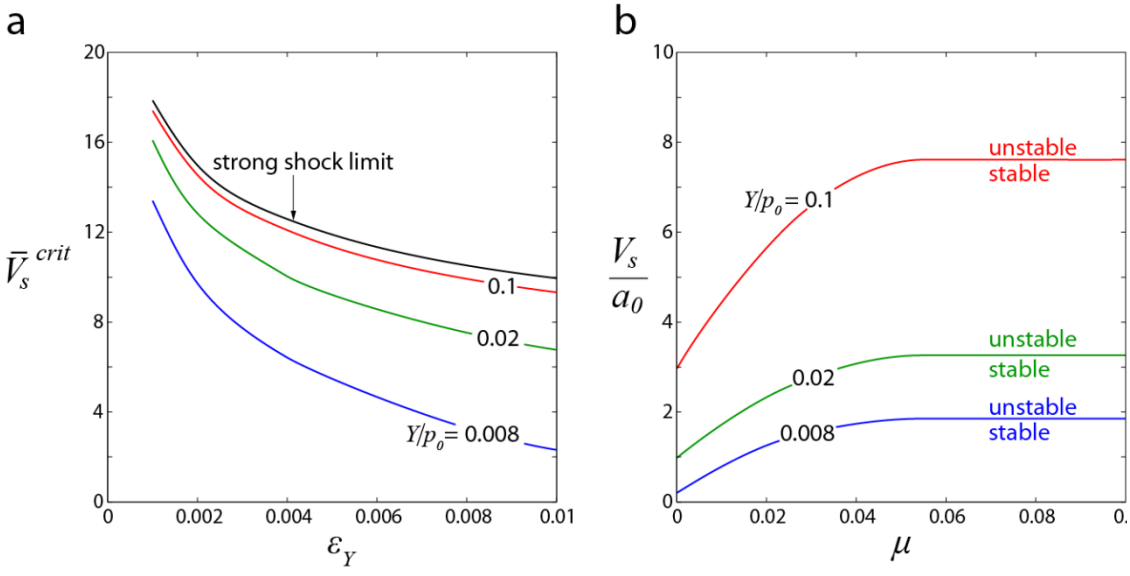

Figure 23: (a) Predictions of the variation of the normalised critical velocity $\bar{V}_s^{crit}$ with ε_Y for a frictionless slug with $\nu = 0.49$, $H/D = 1.4$, $D/\lambda = 3.5$ and $A/\lambda = 0.01$. Results are shown for three choices of the normalised yield strength Y/p_0. (b) The corresponding stability map in $V_s/a_0 - \mu$ space for a slug with $\varepsilon_Y = 0.01$ and three choices of the normalised yield strength Y/p_0.

7.2 Critical velocity to initiate front face instabilities

The conditions required to trigger front face instabilities in these shock loaded granular slugs are a result of complex interactions, viz. the shock loading of the slug to accelerate it, the development of a shocked air region in the front of the accelerating slug and the resultant pressure loading history on the front face. The prediction of the precise evolution of the slug shape and any instability depends on all these details and requires a full numerical calculation such as that shown in Section 7.1. Here an approximate analysis is developed to give indication of the velocity that a slug needs to attain in order to trigger the front face instability.

Consider a slug that has impulsively acquired a velocity V_s. An approximate analysis is sought to determine the critical velocity V_s^{crit} required to trigger instabilities on the front face of such a slug. Recall that a slug moving at constant velocity is equivalent to a slug at rest. Thus, we can employ the calculations of Section 6 for the rear-supported stationary slug to estimate V_s^{crit}. Moreover, in line with the methodology followed earlier in the paper, the case of a slug comprising a J_2 flow theory solid is analysed first and then extended to a frictional Drucker-Prager solid.

The rear-supported slug made from a J_2 flow theory material develops instabilities when loaded by a pressure corresponding to $\overline{Y}_c$ given in Fig. 20b. At the critical velocity V_s^{crit}, the pressure on the front face of the slug is therefore given by $\overline{p}_f = Y/(p_0\overline{Y}_c)$. Substituting this expression in Eq. (7.1) gives an expression for V_s^{crit} in terms of the sonic speed a_0 in ambient (STP) air as

$$\frac{V_s^{\text{crit}}}{a_0} = \frac{1}{\gamma}\left(\frac{Y}{p_0\overline{Y}_c} - 1\right)\left[\frac{2\gamma}{\frac{Y}{p_0\overline{Y}_c}(\gamma+1)+\gamma-1}\right]^{1/2}. \tag{7.3}$$

In the strong shock limit (i.e. in this case $\overline{p}_f = Y/(p_0\overline{Y}_c) \gg 1$) this reduces to

$$\frac{V_s^{\text{crit}}}{a_0} = \left[\frac{2}{\gamma(\gamma+1)}\frac{Y}{p_0\overline{Y}_c}\right]^{1/2}. \tag{7.4}$$

We thus define a normalised critical velocity

$$\overline{V}_s^{\text{crit}} \equiv \frac{V_s^{\text{crit}}}{a_0}\sqrt{\frac{p_0}{Y}}, \tag{7.5}$$

and include in Fig. 23a predictions of $\overline{V}_s^{\text{crit}}$ as a function of ε_Y in the strong shock limit using $\overline{Y}_c$ given in Fig. 20b. Predictions using the full expression, Eq. (7.3), are also included in Fig. 23a for three choices of the normalised yield strength Y/p_0. The strong shock assumption is seen to be valid only for the relatively high granular strengths of $Y/p_0 \geq 0.1$.

The results of Fig. 23a are valid for a slug made from a J_2 flow theory solid. A stability map for front face instabilities in a granular solid can be constructed from the stability map of the rear-supported Drucker-Prager solid as follows. The stability map

for a rear-supported slug comprising a Drucker-Prager material with yield strain $\varepsilon_Y = 0.01$ is given in Fig. 21. The boundary $\overline{Y}_g$ between the stable and unstable regions in $\overline{Y} - \mu$ space then immediately provides the corresponding boundary in $V_s/a_0 - \mu$ space via Eq. (7.1) with $\overline{p}_f = Y/(p_0\overline{Y}_g)$. A front face stability map in $V_s/a_0 - \mu$ space for a granular slug with $\nu = 0.49$, $H/D = 1.4$, $D/\lambda = 3.5$, $A/\lambda = 0.01$ and yield strain $\varepsilon_Y = 0.01$ (i.e. the exact case of the rear-supported granular slug with stability map in Fig. 21) is included in Fig. 23b for three choices of the yield strength Y/p_0. With increasing strength Y/p_0 and friction co-efficient μ, a higher slug velocity is required in order to trigger instabilities on the front face. Such maps provide the demarcation between stable and unstable responses and can be used to explain what explosive loading conditions are required for front face instabilities (referred to as "fingers") to be observed.

8. Concluding remarks

The initiation and growth of surface instabilities in dry sand, and water saturated sand and PTFE sphere slugs loaded by air shocks has been investigated via shock tube experiments and visualised using high-speed photography. In the free-standing state, the surface of the water-saturated sand slug impinged by the shock wave was unstable over all shock pressures considered, while no instability was observed in the dry sand slugs. By contrast, the PTFE sphere slugs were stable at low shock pressures, but exhibited an instability similar to water-saturated sand slugs at high shock pressures. No surface instability was observed on the distal surfaces of the slug (i.e. the front face of the slug) over the range of the shock pressures that were experimentally achievable.

Eulerian fluid/solid interaction calculations with the granular materials modelled as Drucker-Prager solids were shown to adequately predict the stable/unstable responses seen in the experiments. The calculations revealed that instabilities were initiated when the yield condition was activated on the surface of the slug. Stability maps were constructed for granular slugs in $\overline{Y} - \mu$ space where $\overline{Y}$ is the yield strength normalised by the reflected shock pressure and μ the friction co-efficient. The maps show that the shock pressures required to initiate instabilities increased with increasing yield strength, friction co-efficient and decreasing yield strain. In fact, the water-saturated sand was unstable due to its low friction co-efficient while the PTFE sphere slugs became unstable due to their high yield strain in spite to the fact that they had a relatively high friction co-efficient.

The large differences in the densities between atmospheric air and granular materials implied that initiation of the instability on the surface impinged by the shock wave is adequately predicted by directly imposing the reflected shock pressure on the slug surface. Such direct loading calculations were used to establish the parametric dependence of the critical yield strength required to obtain a stable response on slug properties including the material yield strain, surface imperfection amplitude and slug length. Critically the calculations revealed that the instabilities were a result of pressure gradients within the slug due to the initial surface perturbations. Thus, while these instabilities bear similarities to the well-known Rayleigh-Taylor instability (RTI), typical RTI analyses cannot be used for this case since they neglect wave

propagation effects. Shock loading experiments on rear-supported PTFE sphere slugs demonstrated that surface instabilities also occur in this case, albeit at higher shock pressures (here too due to pressure gradients caused by wave propagation effects). Again, simulations were shown to predict the onset of these instabilities with good accuracy.

Instabilities on the front surfaces of the slugs are often observed in explosive loading experiments. However, while such instabilities were not observed in the low pressure experiments conducted here, simulations with high shock pressures (not achievable in the shock apparatus used here) revealed that the front surfaces also become unstable and forms "fingers". This occurs due to pressure loading of the front face of the slug by shock waves initiated by the motion of the slug. We conclude by presenting stability maps with axes of slug velocity and μ for the initiation of the front surface finger-like instabilities in these granular slugs. This study provides a comprehensive treatment of instability criteria for shock loaded granular media in a one-dimensional setting. While such a one-dimensional setting is relatively rare in practise, we anticipate that the key phenomena remain similar in two and three-dimensional settings.

Appendix A: Measurement of granular material properties

The material properties of the three granular slugs listed in Table 1 were measured as follows. The density ρ_{slug} was directly inferred from the weight and volume of the slugs while the Poisson's ratio ν was not directly measured but assumed to be $\nu = 0.49$ based on the usual assumption that the bulk modulus of granular materials is far in excess of their Young's modulus. The yield strength Y, friction angle φ and Young's modulus were measured as follows.

The yield strength was measured using a laboratory miniature vane shear test following ASTM D4648 while the friction angle was measured using the fixed funnel method (ASTM C1444-00) to generate a cone of the granular material. The friction angle was then inferred from the ratio of the height to the half width of the base of the cone. The friction angle as measured for the dry sand was relatively low (in the range $21^o - 25^o$ with an average of 23^o over 10 independent tests) compared to some values reported in the literature. However, we emphasize that the main conclusions of the study remain unchanged even if the friction angle were increased as the unstable/stable boundary is independent of the friction co-efficient for $\mu > 0.005$ (Fig. 11b).

A constrained compression test using a double plunger apparatus (Uth and Deshpande, 2014) was conducted to measure the Young's modulus of the granular materials. The so-called constrained modulus S was measured from the unloading slope of the constrained compression stress versus strain curve and the Young's modulus then obtained from

$$E = \frac{S(1+\nu)(1-2\nu)}{1-\nu}. \tag{A1}$$

It is evident from Eq. (A1) that the inferred E depends on the choice of ν. The results presented in the paper are reasonably independent of ν over the range $0.28 \leq \nu \leq 0.49$ so long as the Young's modulus was inferred consistently using (A1).

Appendix B: Relation between stability criteria of frictionless and frictional materials

Recall that $\overline{Y}_0(\hat{p}_r,\nu)$ or equivalently $\overline{Y}_c(\varepsilon_Y,\nu)$ fully describes the stability map and we thus recast the stability condition, Eq. (4.4), in terms of $\overline{Y}_c(\varepsilon_Y,\nu)$ rather than $\overline{Y}_c(\hat{p}_r,\nu)$.

The stable/unstable boundary in $\overline{Y} - \mu$ space is given by Eq. (4.4) as

$$\overline{Y} \geq \overline{Y}_0(\hat{p}_r,\nu) - \mu. \tag{B1}$$

We re-write Eq. (B1) as

$$\varepsilon_Y \geq \left[\overline{Y}_0(\hat{p}_r,\nu) - \mu\right]\hat{p}_r, \tag{B2}$$

where $\varepsilon_Y \equiv Y/E$ is the yield strain of the granular material with friction co-efficient μ. Next we define the yield strain $\varepsilon_0 = \overline{Y}_0\hat{p}_r$ of the frictionless material that is just stable when subjected to a loading $\hat{p}_r$ and rewrite Eq. (B2) as

$$\varepsilon_Y \geq \varepsilon_0\left[1 - \frac{\mu}{\overline{Y}_0(\hat{p}_r,\nu)}\right], \tag{B3}$$

where the equality corresponds to the case of a just stable response. Using the transformation $\hat{p}_r = \varepsilon_0/\overline{Y}_0$ we recast Eq. (B3) as

$$\varepsilon_Y \geq \varepsilon_0\left[1 - \frac{\mu}{\overline{Y}_c(\varepsilon_0,\nu)}\right]. \tag{B4}$$

Given the functional form $\overline{Y}_c(\varepsilon_0,\nu)$ (see for example Fig. 10b) along with μ and ε_Y we can determine the critical value ε_0 that satisfies the equality in Eq. (B4). The critical non-dimensional yield strength $\overline{Y}_g$ required for stability of the frictional solid then follows as $\overline{Y}_g(\nu,\varepsilon_Y,\mu) = \overline{Y}_c(\varepsilon_0,\nu)\varepsilon_Y/\varepsilon_0(\nu,\varepsilon_Y,\mu)$.

Acknowledgements

The work was supported by the Defense Advanced Projects Agency under grant number W91CRB-11-1-0005 (Program manager, Dr. J. Goldwasser).

References

Abrahamson, G.R., Goodier, J.N., 1966. Dynamic flexural buckling of rods within an axial plastic compression wave. *J. Appl. Mech.* 33, 241–247.

Bolton, M.D., 1991. *A Guide to Soil Mechanics*, Macmillan Education Ltd.

Cole, R.H., 1948. *Underwater explosions*, Princeton University Press.

Drucker, D. C., Prager, W., 1952. Soil mechanics and plastic analysis for limit design. *Quarterly of Applied Mathematics*, 10, 157–165.

Drucker, D.C., 1980. A further look at Rayleigh-Taylor and other surface instabilities in solids, *Ing.-Arch*. 49, 361–367.

Frost, D. L., Zhang, F., 2006. The nature of heterogeneous blast. *Proc. 19th Int. Symp. Military Aspects of Blast and Shock.*

Frost, D.L., Goroshin, S., Zhang, F., 2010. Jet formation during explosive particle dispersion. *Proc. 21st Military Aspects of Blast and Shock.*

Frost, D.L., Grégoire, Y., Goroshin, S., Zhang, F., 2011. Interfacial instabilities in explosive gas- particle flows, *Proc. 23rd Int. Coll. Dynamics of Explosions and Reactive Systems.*

Frost, D.L., Grégoire, Y., Petel, O., Goroshin, S., Zhang, F., 2012. Particle jet formation during explosive dispersal of solid particles, *Phys. Fluids.* 24, 091109.

Grady, D.E., 1982. Local inertial effects in dynamic fragmentation, *J. Appl. Phys.* 53, 322–325.

Keyner, A., Dharmasena, K., Williams, K., Deshpande, V.S., Wadley, H.N.G., 2016. Deformation of an edge clamped plate by localized impact of high momentum sand, *Int. J. Impact. Eng*., submitted.

Liepmann, H.W., Roshko, A., 2001. *Elements of gasdynamics*, Dover Publications.

Liu, T., Wadley, H.N.G., Deshpande, V.S., 2014. Dynamic compression of foam supported impacted by high velocity soil, *Int. J. Impact. Eng*., 63, 88-105.

Milne, A.M., Parrish, C., Worland, I., 2010. Dynamic fragmentation of blast mitigants, *Shock Waves*. 20, 41–51.

Park, S., Uth, T., Fleck, N.A., Wadley, H.N.G., Deshpande, V.S., 2013. Sand column impact with a rigid target, *Int. J. Impact. Eng*. 62, 229-242.

Piriz, A.R., López Cela, J.J., Tahir, N.A., 2009. Linear analysis of incompressible Rayleigh-Taylor instability in solids, *Phys. Rev. E*., 80, 046305.

Richtmyer, R.D., 1960. Taylor instability in shock acceleration of compressible fluids. *Comm. Pure Appl. Math.* 8:297–319.

Ripley, R.C., Donahue, L., Zhang, F., 2012. Jetting instabilities of particles from explosive dispersal *AIP Conf. Proc.* 1426 1615–1618.

Ritzel, D.V., Ripley, R. C., Murray, S.B., Anderson, J., 2007. Near field blast phenomenology of thermobaric explosions. *Proc. 26th Int. Symp. Shock Waves.* 1:305–310.

Rodriguez, V., Saurel, R., Jourdan, G., Houas, L. 2014. External front instabilities induced by a shocked particle ring, *Phys. Rev. E.* 90, 043013.

Taylor, G.I., 1940. Pressures on solid bodies near an explosion, *In the scientific papers of G.I. Taylor (1963)*, Edited by G.K. Batchelor, Cambridge University Press.

Taylor, G.I., 1950. The instability of liquid surfaces when accelerated in a direction perpendicular to their planes, *Proc. Roy. Soc. A*. 201,192–196.

Uth, T., Deshpande, V.S., 2014. Response of clamped sandwich beams subjected to high- velocity impact by sand slugs, *Int. J. Impact. Eng*. 69, 165-181.

Xu, T., Lien, F-S., Ji, H., Zhang, F. 2013. Formation of particle jetting in a cylindrical shock tube, *Shock Waves*. 23 619–634.

Zhang, F., Yoshinaka, A., Ripley, R., 2010. Hybrid detonation waves in metalized explosive mixtures. *Proc. 14th Int. Detonation Symp.* 714–723.

Zhang, F., Findlay, R., Anderson, J., Ripley, R. 2013. Large scale unconfined gasoline spray detonation, *Proc. Int. Coll. Dynamics of Explosions and Reactive Systems.*